This is a repository copy of *Interplay between fluctuation driven toroidal axisymmetric flows and resistive ballooning mode turbulence*.

White Rose Research Online URL for this paper:
https://eprints.whiterose.ac.uk/id/eprint/139986/

Version: Accepted Version

Article:

Interplay between fluctuation driven toroidal axisymmetric flows and resistive ballooning mode turbulence

H. Seto,[1, a)] X.Q. Xu,[2] B.D. Dudson,[3] and M. Yagi[1]

[1)]*National Institutes for Quantum and Radiological Science and Technology, Rokkasho, Aomori 039-3212, Japan*

[2)]*Lawrence Livermore National Laboratory, Livermore, California 94550, USA*

[3)]*York Plasma Institute, Department of Physics, University of York, Heslington, York YO10 5DD, UK*

An interplay between fluctuation driven toroidal axisymmetric flows (convective cell modes) and resistive ballooning mode turbulence after the pedestal collapse is numerically studied by a four-field reduced MHD model in BOUT++ framework. The strong flow shear suppresses the radial transport of pressure filaments and the pressure profile in the pedestal region is partially recovered. As a result, a secondary instability is quasi-linearly excited, which yields a secondary collapse. The subsequent damped oscillation is also analyzed by phase diagram analysis.

[a)]seto.haruki@qst.go.jp

I. INTRODUCTION

In future tokamak fusion reactors such as ITER[1] and DEMO[2,3], the high-confinement mode discharge[4] is a baseline operation scenario while intermittent large heat fluxes released by edge localized modes (ELMs)[5] should be avoided or mitigated to levels low enough to remain within heat load constraints on plasma facing components. One of the critical issues is therefore to understand the nonlinear dynamics underlying the ELM crash and resultant energy loss process. Several nonlinear MHD codes such as BOUT[6–9], M3D[10], NIMROD[11,12], JOREK[13–18], M3D-C1[19] and BOUT++[20–25] have therefore been developed and provided qualitative understanding of the nonlinear dynamics of ELMs.

The fluctuation driven toroidal axisymmetric flows are generally called "convective cell" modes[26], especially "zonal flows"[27] for $(m = 0, n = 0)$ where m and n are the poloidal and toroidal mode numbers respectively. Hereafter, (m, n) indicates Fourier mode with mode numbers m and n. In this paper, we simply abbreviate "CCs" and "ZFs" for $n = 0$ $E \times B$ flows. It is well-known that ZFs are not generated by the modes with MHD parity due to the cancellation between Reynolds stress and Maxwell stress[28], therefore, kinetic effects and/or two-fluid effects play a role for parity breaking which contributes to the generation mechanism. JOREK simulations[13,15,18] show that the strongly sheared ZFs generated via the residual of force balance mainly described by the Maxwell stress and the toroidal curvature, which suppress the transport. However, the generation mechanism of CCs and its impact on transport during ELMs are not yet well understood compared to the drift wave turbulence[28].

In the BOUT++ framework, there was a limitation to handle CCs in previous work[21–23] which is attributed to the flute ordered one-dimensional Poisson solver for CCs. Recently a two-dimensional Poisson solver in the quasi-ballooning coordinate system[20] for CCs has been developed and introduced in Hermes code for self-consistent edge turbulence simulations[29]. Hermes code belongs to the chain of BOUT++ code solving three-dimensional plasma edge turbulence physics with conservative finite differences while BOUT++ code solves three-dimensional plasma edge MHD physics with finite differences in the gradient form. We have implemented the two-dimensional Poisson solver for CCs in the gradient form in BOUT++ framework at the first time. Detail descriptions on the quasi-ballooning coordinate system and the two-dimensional Poisson solver are given in Appendix A and B respectively.

In this paper, we report nonlinear simulations of resistive ballooning mode (RBM) tur-

bulence after pedestal collapse using a four-field reduced MHD model[30], with multi-helicity initial perturbations in a shifted circular equilibrium taking account of CCs. Here we use the terminology "pedestal collapse" instead of ELM crash, since we consider RBMs instead of peeling-ballooning mode in this simulation. The interplay between CCs and RBM turbulence is investigated. It is found that the secondary collapse is triggered by a secondary instability accompanied by damped oscillations, based on energy transfer rate analyses, as well as spatio-temporal analyses and phase diagram analyses.

The remainder of this paper is organized as the following. The four-field model is described in Section II. Section III presents a shifted circular equilibrium and its linear stability properties using the four-field model. In Section IV, an impact of CCs generated by middle-n to high-n RBM turbulence on the secondary collapse and the subsequent transport are reported. Finally this paper is summarized in Section V.

II. FOUR-FIELD TWO-FLUID MODEL

A scale separated four-field reduced MHD model consisting of evolution equations for vorticity ϖ, magnetic potential $A_\parallel$, plasma pressure p and ion parallel flow $v_\parallel$ is employed. We adopt a rather simple model with a shifted circular equilibrium without sources, sinks, an equilibrium radial electric field, an equilibrium parallel flow or SOL transport, to identify the detailed energy channel between CCs and RBM turbulence. The four-field model is normalized with poloidal Alfvén units with the plasma major radius at the magnetic axis R_{ax}, the magnetic field intensity at the magnetic axis B_{ax}, the reference ion number density n_{i} and the poloidal Alfvén time $t_A = R_{\mathrm{ax}}/V_A$ (See Table II), where $V_A = B_{\mathrm{ax}}/\sqrt{\mu_0 n_{\mathrm{i}} m_{\mathrm{i}}}$ is the Alfvén velocity, μ_0 is the permittivity in vacuum, n_{i} is the reference ion number density, m_{i} is the ion mass respectively. It should be noted that the vorticity has dimensions $B_{\mathrm{ax}}^{-1} t_A^{-1}$ rather than t_A^{-1} in this paper. The model[30,31] is given by

$$\frac{\partial \varpi_1}{\partial t} = -[F_0, \varpi_1] - [F_1, \varpi_0] - [F_1, \varpi_1] - \nabla_\parallel J_{\parallel 1} + B_0 \left[A_{\parallel 1}, \frac{J_{\parallel 0}}{B_0}\right] + \mathcal{K}(p_1)$$
$$+ \mathcal{G}(p_0, F_1) + \mathcal{G}(p_1, F_0) + \mathcal{G}(p_1, F_1) + \mu_\parallel \partial_{\parallel 0}^2 \varpi_1 + \mu_\perp \nabla_\perp^2 \varpi_1 \tag{1}$$

$$\frac{\partial p_1}{\partial t} = -[\phi_1, p_0] - [\phi_1, p_1] - 2\beta_* \mathcal{K}(\phi_1) - \beta_* \nabla_\parallel \left(v_{\parallel 1} + d_{\mathrm{i}} J_{\parallel 1}\right) + \chi_\parallel \partial_{\parallel 0}^2 p_1 + \chi_\perp \nabla_\perp^2 p_1 \tag{2}$$

$$\frac{\partial A_{\parallel 1}}{\partial t} = -\partial_\parallel \phi_1 + \delta_{\mathrm{e}} \partial_\parallel p_1 - \delta_{\mathrm{e}} \left[A_{\parallel 1}, p_0\right] + \eta J_{\parallel 1} - \lambda \nabla_\perp^2 J_{\parallel 1} \tag{3}$$

3

$$\frac{\partial v_{\|1}}{\partial t} = - \left[\phi_1, v_{\|1}\right] - \frac{1}{2}\left(\partial_\| p_1 - \left[A_{\|1}, p_0\right]\right) + \nu_\perp \nabla_\perp^2 v_{\|1} \tag{4}$$

$$\mathcal{G}(f, g) = \frac{\delta_i}{2}\left\{\left[f, \nabla \cdot \left(\frac{\nabla_\perp g}{B_0^2}\right)\right] + \left[g, \nabla \cdot \left(\frac{\nabla_\perp f}{B_0^2}\right)\right] + \nabla \cdot \left(\frac{\nabla_\perp [f, g]}{B_0^2}\right)\right\},$$

$$\varpi = \nabla \cdot \left(\frac{\nabla F}{B_0^2}\right), \quad F = \phi + \delta_i p, \quad \phi = \phi_1, \quad p = p_0 + p_1,$$

$$\boldsymbol{B} = \boldsymbol{B}_0 + \nabla A_{\|1} \times \boldsymbol{b}_0, \quad J_\| = J_{\|0} + J_{\|1}, \quad \delta_i = \delta_e = \frac{d_i}{4}, \quad d_i = \frac{c}{R_{\text{ax}}}\sqrt{\frac{m_i \varepsilon_0}{n_i Z_i e^2}},$$

where evolving quantities have been separated into an equilibrium component with subscript 0 and a perturbed component with subscript 1 and terms involving only equilibrium quantities are removed from the system. Here $[f, g] = (\boldsymbol{b}_0 \times \nabla_\perp f \cdot \nabla_\perp g)/B_0$, $\nabla_\perp f = (\nabla - \boldsymbol{b}_0 \partial_{\|0})f$, $\partial_{\|0} f = \boldsymbol{b}_0 \cdot \nabla f$, $\nabla_\| f = B_0 \partial_\|(f/B_0)$, $\partial_\| f = \partial_{\|0} f - [A_{\|1}, f]$, $\mathcal{K}(f) = (\boldsymbol{b}_0 \times \boldsymbol{\kappa}_0 \cdot \nabla f)/B_0$ for any f and g, the unit vector along the field line $\boldsymbol{b}_0$, the equilibrium magnetic curvature $\boldsymbol{\kappa}_0 = \boldsymbol{b}_0 \cdot \nabla \boldsymbol{b}_0$, the generalized flow potential F, the electrostatic potential ϕ, the perturbed parallel current $J_{\|1} = \nabla_\perp^2 A_{\|1}$, the compression parameter $\beta_* = B_0^2/[0.5 + B_0^2/(\Gamma p_0)]$, the adiabatic constant $\Gamma = 5/3$, the operator describing the ion diamagnetic effect $\mathcal{G}$, the factor for ion diamagnetism δ_i, the factor for electron diamagnetism δ_e, the ion skin depth d_i, the speed of light in vacuum c, the permeability in vacuum ε_0, the effective ion charge number Z_i, the elementary charge e, the perpendicular viscosity for vorticity $\mu_\perp$, the parallel viscosity for vorticity $\mu_\|$, the resistivity η, the hyper resistivity λ, the perpendicular diffusivity $\chi_\perp$, the parallel diffusivity $\chi_\|$ and the perpendicular viscosity for parallel flow $\nu_\perp$ respectively.

In the derivation of Eqs. (1)-(4), the Boussinesq approximation with a flat ion density profile n_i, the iso-thermal approximation $T_e = T_i$ and the charge quasi-neutrality with the effective ion charge number $Z_i = 1$ have also been assumed and the electron inertia effect has been neglected for simplicity. For ion diamagnetism model, only the lowest order finite Larmor radius (FLR) effect in the Chang-Callen ion gyroviscous model[31] have been introduced in Eq. (1) like the original BOUT[7] and BOUT++[21,22]. The present four-field model therefore includes non-ideal effects such as two-fluid effects including the lowest order ion diamagnetism and electron drift wave, resistivity, hyper-resistivity and flow compression.

For energy transfer rate analyses, multiplying the vorticity equation Eq. (1) by $-F_1$, the energy equation Eq. (2) by $p_1/2\beta_*$, Ohm's law Eq. (3) by $-J_{\|1}$ and the ion parallel flow

TABLE I. Normalizations in this paper

Physical quantity	Symbol	Normalization
time	t	t_A
vorticity	ϖ	$B_{ax}^{-1} t_A^{-1}$
pressure	p	$B_{ax}^2 (2\mu_0)^{-1}$
magnetic potential	$A_\parallel$	$B_{ax} R_{ax}$
ion parallel flow	$v_\parallel$	V_A
electrostatic potential	ϕ	$V_A B_{ax} R_{ax}$
parallel current	$J_\parallel$	$-B_{ax}(\mu_0 R_{ax})^{-1}$
resistivity	η	$\mu_0 V_A R_{ax}$
hyper resistivity	λ	$\mu_0 V_A R_{ax}^3$

Eq. (4) by $v_{\parallel_1}$, we get a set of equations for energies as

$$
\begin{aligned}
\frac{\partial W_k}{\partial t} =& \langle F_1\left[F_0, \varpi_1\right]\rangle_V + \langle F_1\left[F_1, \varpi_0\right]\rangle_V + \langle F_1\left[F_1, \varpi_1\right]\rangle_V \\
& - \langle F_1 \mathcal{G}\left(p_0, F_1\right)\rangle_V - \langle F_1 \mathcal{G}\left(p_1, F_0\right)\rangle_V - \langle F_1 \mathcal{G}\left(p_1, F_1\right)\rangle_V \\
& + \langle F_1 \nabla_{\parallel_0} J_{\parallel_1}\rangle_V - \langle F_1 B_0\left[A_{\parallel_1}, \frac{J_{\parallel_0}}{B_0}\right]\rangle_V - \langle F_1 B_0\left[A_{\parallel_1}, \frac{J_{\parallel_1}}{B_0}\right]\rangle_V \\
& - \langle F_1 \mathcal{K}(p_1)\rangle_V - \langle \mu_\parallel \left|\partial_{\parallel_0} F_1\right|^2\rangle_V - \langle \mu_\perp \left|\nabla_\perp F_1\right|^2\rangle_V,
\end{aligned} \tag{5}
$$

$$
\begin{aligned}
\frac{\partial W_p}{\partial t} =& -\langle \frac{p_1\left[\phi_1, p_0\right]}{2\beta_*}\rangle_V - \langle \frac{p_1\left[\phi_1, p_1\right]}{2\beta_*}\rangle_V + \langle \frac{\chi_\parallel p_1 \partial_{\parallel_0}^2 p_1}{2\beta_*}\rangle_V + \langle \frac{\chi_\perp p_1 \nabla_\perp^2 p_1}{2\beta_*}\rangle_V \\
& - \langle p_1 \mathcal{K}\left(\phi_1\right)\rangle_V - \langle \frac{1}{2} p_1 \nabla_{\parallel_0} v_{\parallel_1}\rangle_V + \langle \frac{1}{2} p_1 B_0\left[A_{\parallel_1}, \frac{v_{\parallel_1}}{B_0}\right]\rangle_V \\
& - \langle \frac{d_i}{2} p_1 \nabla_{\parallel_0} J_{\parallel_1}\rangle_V + \langle \frac{d_i}{2} p_1 B_0\left[A_{\parallel_1}, \frac{J_{\parallel_1}}{B_0}\right]\rangle_V,
\end{aligned} \tag{6}
$$

$$
\begin{aligned}
\frac{\partial W_m}{\partial t} =& \langle J_{\parallel_1}\left[\phi_1, A_{\parallel_1}\right]\rangle_V + \langle J_{\parallel_1} \partial_{\parallel_0} \phi_1\rangle_V + \langle \delta_e J_{\parallel_1}\left[A_{\parallel_1}, p_0\right]\rangle_V - \langle \delta_e J_{\parallel_1} \partial_{\parallel_0} p_1\rangle_V \\
& + \langle \delta_e J_{\parallel_1}\left[A_{\parallel_1}, p_1\right]\rangle_V - \langle \eta J_{\parallel_1}^2\rangle_V - \langle \lambda \left|\nabla_\perp J_{\parallel_1}\right|^2\rangle_V,
\end{aligned} \tag{7}
$$

$$
\begin{aligned}
\frac{\partial W_v}{\partial t} =& -\langle v_{\parallel_1}\left[\phi_1, v_{\parallel_1}\right]\rangle_V - \langle \frac{1}{2} v_{\parallel_1} \partial_{\parallel_0} p_1\rangle_V + \langle \frac{1}{2} v_{\parallel_1}\left[A_{\parallel_1}, p_0\right]\rangle_V + \langle \frac{1}{2} v_{\parallel_1}\left[A_{\parallel_1}, p_1\right]\rangle_V \\
& - \langle \nu_\perp \left|\nabla_\perp v_{\parallel_1}\right|^2\rangle_V,
\end{aligned} \tag{8}
$$

where $W_k = \langle \left|\nabla_\perp F_1\right|^2 / 2B_0^2\rangle_V$ is the perpendicular kinetic energy, $W_p = \langle p_1^2/4\beta_*\rangle_V$ is the internal energy, $W_m = \langle \left|\nabla_\perp A_{\parallel_1}\right|^2 /2\rangle_V$ is the magnetic energy, $W_v = \langle v_{\parallel_1}^2/2\rangle_V$ is the parallel kinetic energy and $\langle f\rangle_V = \int_V f dV$ represents the volume integral over the entire simulated

domain respectively. Here, the absence of boundary fluxes has been assumed in the derivation of Eqs. (5)-(8). It should be noted that the system described with Eqs. (1)-(4) has a complete set of energy transfer channels, while some contributions from equilibrium fields such as $\langle F_1 [F_0, \varpi_1] \rangle_V$ can be effective sources. In other words all nonlinear cross terms in Eqs. (5)-(8) are canceled out with other terms so that the total energy should be conserved after nonlinear relaxation if numerical dissipation terms, effective sources and boundary fluxes are negligibly small.

The equation for the (m, n) component of internal energy is expressed by

$$
\begin{aligned}
\frac{d}{dt} W_p^{(m,n)} =& T_{p,E\times B}^{(m,n)} + T_{p,D}^{(m,n)} + T_{p,CMP}^{(m,n)}, \\
T_{p,E\times B}^{(m,n)} =& -\langle \frac{p_{1(m,n)} [\phi_1, p_1]}{2\beta_*} \rangle_V - \langle \frac{p_{1(m,n)} [\phi_1, p_0]}{2\beta_*} \rangle_V, \\
T_{p,D}^{(m,n)} =& \langle \frac{\chi_\parallel p_{1(m,n)} \partial_{\parallel 0}^2 p_1}{2\beta_*} \rangle_V + \langle \frac{\chi_\perp p_{1(m,n)} \nabla_\perp^2 p_1}{2\beta_*} \rangle_V \\
\simeq& -\langle \frac{\chi_\parallel}{2\beta_*} \left| \partial_{\parallel 0} p_{1(m,n)} \right|^2 \rangle_V - \langle \frac{\chi_\perp}{2\beta_*} \left| \nabla_\perp p_{1(m,n)} \right|^2 \rangle_V, \\
T_{p,CMP}^{(m,n)} =& -\langle p_{1(m,n)} \mathcal{K}(\phi_1) \rangle_V - \langle \frac{1}{2} p_{1(m,n)} \nabla_{\parallel 0} v_{\parallel 1} \rangle_V + \langle \frac{1}{2} p_{1(m,n)} B_0 \left[A_{\parallel 1}, \frac{v_{\parallel 1}}{B_0} \right] \rangle_V \\
& -\langle \frac{d_i}{2} p_{1(m,n)} \nabla_{\parallel 0} J_{\parallel 1} \rangle_V + \langle \frac{d_i}{2} p_{1(m,n)} B_0 \left[A_{\parallel 1}, \frac{J_{\parallel 1}}{B_0} \right] \rangle_V,
\end{aligned}
$$

(9)

where $W_p^{(m,n)}$ is the (m, n) component of internal energy, $T_{p,E\times B}^{(m,n)}$ is the (m, n) component of energy transfer rate by $E \times B$ convection, $T_{p,D}^{(m,n)}$ by diffusion terms, $T_{p,CMP}^{(m,n)}$ by compression effects respectively.

Similarly, the equation for the (m, n) component of perpendicular kinetic energy is expressed by

$$
\begin{aligned}
\frac{d}{dt} W_k^{(m,n)} =& T_{k,R}^{(m,n)} + T_{k,ID}^{(m,n)} + T_{k,J\times B}^{(m,n)} + T_{k,C}^{(m,n)} + T_{k,D}^{(m,n)}, \\
T_{k,R}^{(m,n)} =& \langle F_{1(m,n)} [F_0, \varpi_1] \rangle_V + \langle F_{1(m,n)} [F_1, \varpi_0] \rangle_V + \langle F_{1(m,n)} [F_1, \varpi_1] \rangle_V, \\
T_{k,ID}^{(m,n)} =& -\langle F_{1(m,n)} \mathcal{G}(p_0, F_1) \rangle_V - \langle F_{1(m,n)} \mathcal{G}(p_1, F_0) \rangle_V - \langle F_{1(m,n)} \mathcal{G}(p_1, F_1) \rangle_V, \\
T_{k,J\times B}^{(m,n)} =& T_{k,LB}^{(m,n)} + T_{k,K}^{(m,n)} + T_{k,M}^{(m,n)} \\
T_{k,LB}^{(m,n)} =& \langle F_{1(m,n)} \nabla_{\parallel 0} J_{\parallel 1} \rangle_V, \quad T_{k,K}^{(m,n)} = -\langle F_{1(m,n)} B_0 \left[A_{\parallel 1}, \frac{J_{\parallel 0}}{B_0} \right] \rangle_V, \\
T_{k,M}^{(m,n)} =& -\langle F_{1(m,n)} B_0 \left[A_{\parallel 1}, \frac{J_{\parallel 1}}{B_0} \right] \rangle_V, \quad T_{k,C}^{(m,n)} = -\langle F_{1(m,n)} \mathcal{K}(p_1) \rangle_V, \\
T_{k,D}^{(m,n)} =& -\langle \mu_\parallel \left| \partial_{\parallel 0} F_{1(m,n)} \right|^2 \rangle_V - \langle \mu_\perp \left| \nabla_\perp F_{1(m,n)} \right|^2 \rangle_V,
\end{aligned}
$$

(10)

where $W_k^{(m,n)}$ is the (m,n) component of perpendicular kinetic energy, $T_{k,R}^{(m,n)}$ is the (m,n) component of the energy transfer rate by the Reynolds stress, $T_{k,ID}^{(m,n)}$ by the ion diamagnetic flow stress, $T_{k,J\times B}^{(m,n)}$ by $\boldsymbol{J} \times \boldsymbol{B}$ force including the line-bending force $T_{k,LB}^{(m,n)}$, the kink term $T_{k,K}^{(m,n)}$ and the Maxwell stress $T_{k,M}^{(m,n)}$, $T_{k,C}^{(m,n)}$ by the toroidal curvature term and $T_{k,D}^{(m,n)}$ by the viscosity terms respectively.

In the BOUT++ code, Eqs. (1)-(4) are solved in the quasi-ballooning coordinate system (ψ, y, z), where ψ is the radial label and y is the parallel label and z is the binormal label respectively. Details of the quasi-ballooning coordinate system are briefly reviewed in Appendix A. Differencing methods used are fourth-order central differencing in ψ direction and y direction and FFT in z direction except for the Laplacian operator $\nabla_\perp^2$ and the Poisson solvers. For the Laplacian operator and the Poisson solvers, second-order central differencing in ψ direction and y direction and FFT in z direction are employed, where Poisson solvers used in the present work are also explained in Appendix B. The resultant differential equation is implicitly solved with Newton-Krylov BDF method provided by the SUNDIALS library[32,33]. The radial boundary conditions used are $\partial_\psi \varpi_1 = 0$, $\partial_\psi p_1 = 0$, $\partial_\psi A_{\|1} = 0$, $\partial_\psi V_{\|1} = 0$, $\partial_\psi \phi_1 = 0$ and $\partial_\psi J_{\|1} = 0$ on the inner radial boundary and $\varpi_1 = 0$, $p_1 = 0$, $\nabla_\perp^2 A_{\|1} = 0$, $V_{\|1} = 0$, $\phi_1 = 0$ and $J_{\|1} = 0$ on the outer radial boundary respectively. Hereafter, we will omit the subscript "1" to express the perturbed part of field variables, where this does not cause.

III.   MHD EQUILIBRIUM AND ITS LINEAR STABILITY AGAINST FOUR-FIELD MODEL

For RBM turbulence simulations after pedestal collapse, a shifted circular equilibrium (cbm18_dens4) is employed, which is one of a series of equilibria (cbm18_series)[19] generated by the TOQ equilibrium code[34,35]. The pressure, parallel current on the outer mid-plane as well as safety factor profile over the radial domain labeled with the normalized ψ ($0.4 \le \psi \le 1.2$) are shown in Fig. 1, where these quantities have been normalized by the poloidal Alfvén units with $R_{\mathrm{ax}} = 3.5$ [m], $B_{\mathrm{ax}} = 2.0$ [T], $n_i = 1.0 \times 10^{19}$ [m^{-3}] and the deuterium mass. It should be noted that the definition of the last closed flux surface (LCFS) $\psi = 1.0$ has an arbitrarity since there are no X-points or limiters and neither the topology of flux surfaces nor boundary conditions change at $\psi = 1.0$ in this equilibrium.
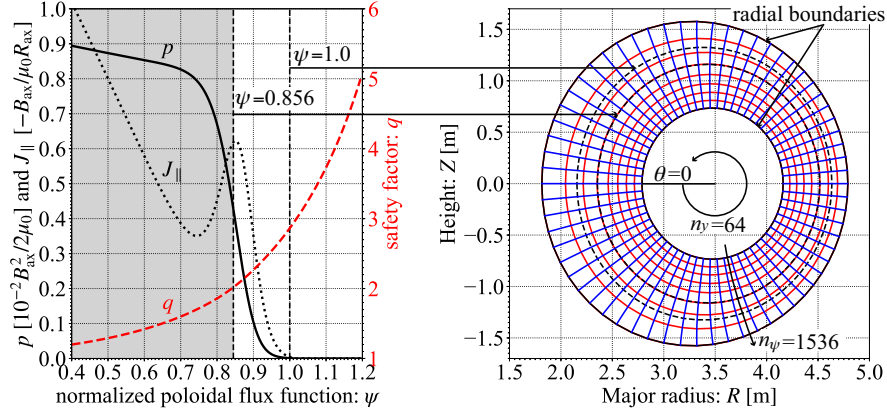
7

FIG. 1. Shifted circular equilibrium (cbm18_dens4) profiles and mesh: pressure (black solid), parallel current (black dotted) and safety factor (red dashed) profiles on the outer mid-plane (left) and poloidal cross-section of mesh the radial grid of which is coarsened for clarity (right).

The shaded area in Fig. 1 represents the radial domain $0.4 \leq \psi \leq 0.856$ of volume over which the released energy ΔW_{ped} and the internal energy W_{ped} are defined by,

$$\Delta W_{\mathrm{ped}} = - \int_{V_{\mathrm{ped}}} p_1 dV, \quad W_{\mathrm{ped}} = \int_{V_{\mathrm{ped}}} p_0 dV, \tag{11}$$

where $\psi = 0.856$ is the radial peak position of pressure gradient. Then, the energy loss is introduced by the ratio of them $\Delta W_{\mathrm{ped}}/W_{\mathrm{ped}}$[21].

The linear stability for ideal ballooning mode (IBM) and RBM are shown in Fig. 2. Here, we have set the resistivities to $\eta = 10^{-8}$ $[\mu_0 V_A R_{\mathrm{ax}}]$ $(= 4.3 \times 10^{-7}$ $[\Omega\mathrm{m}])$ and $\lambda = 10^{-12}$ $[\mu_0 V_A R_{\mathrm{ax}}^3]$ $(= 5.3 \times 10^{-10}$ $[\Omega\mathrm{m}^3])$ and also employed the following numerical dissipation both in the perpendicular directions $\mu_\perp = \chi_\perp = \nu_\perp = 10^{-7}$ $[R_{\mathrm{ax}}^2 t_A^{-1}]$ $(= 3.4 \times 10^0$ $[\mathrm{m}^2/\mathrm{s}])$ and in the parallel direction $\mu_\parallel = \chi_\parallel = 10^{-1}$ $[R_{\mathrm{ax}}^2 t_A^{-1}]$ $(= 3.4 \times 10^6$ $[\mathrm{m}^2/\mathrm{s}])$ respectively for numerical stability.

For numerical efficiency of linear analyses, only $1/n$-th of the annular torus with the radial grid points $n_\psi = 1536$, the parallel grid points $n_y = 64$ and the binormal grid points $n_z = 32$ is employed for each toroidal mode number n. The growth rate of n-mode is therefore evaluated as the fundamental mode in the $1/n$-th annular wedge torus. According to Ref. 20, the effective poloidal resolution for toroidal mode number n is roughly estimated by $n_\theta \simeq q n n_z = m_{\mathrm{res}} n_z$. This resolution is high enough to resolve the poloidal sub-harmonics of IBM and RBM, where $m_{\mathrm{res}} = nq$ is the resonant poloidal mode number for the toroidal mode number n on the rational q-surface.
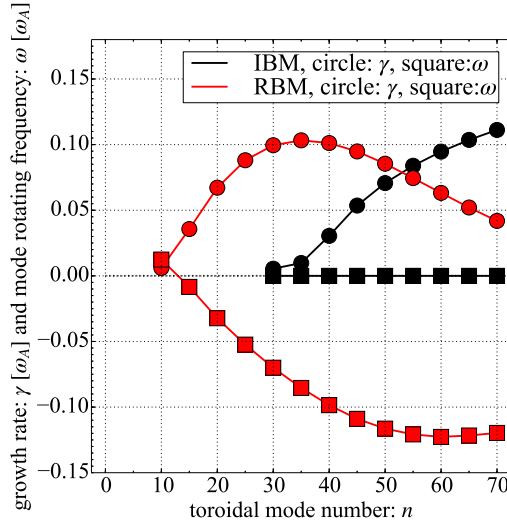
FIG. 2. Linear growth rate and mode rotating frequency of IBM (black) and RBM (red) versus toroidal mode number.

One can find that for RBM, the toroidal modes $n \geq 10$ are unstable and $n = 35$ mode is the most unstable one with $\gamma = 1.03 \times 10^{-1} [\omega_A]$, where $\omega_A = t_A^{-1}$ is the poloidal Alfvén frequency. The toroidal modes larger than $n = 60$ are introduced as an energy sink for nonlinear simulations.

For resistivity and hyper resistivity, we have chosen the hyper-resistivity to be $\lambda/\eta = 10^{-4}$, which is the maximum value estimated in Ref. 22. With these parameters, the resistive current sheet width Δ_η can be estimated as $\Delta_\eta \simeq \sqrt{\eta/\gamma_{\mathrm{IBM}}} = 3.0 \times 10^{-4} [R_{\mathrm{ax}}] (= 1.1 [\mathrm{mm}])$ and the hyper resistive current sheet width Δ_λ as $\Delta_\lambda \simeq (\lambda/\gamma_{\mathrm{PB}})^{1/4} = 1.7 \times 10^{-3} [R_{\mathrm{ax}}] (= 6.1[\mathrm{mm}])$ for the second harmonics of the most unstable mode $(n = 70)$ with $\gamma_{\mathrm{IBM}} = 1.11 \times 10^{-1} [\omega_A]$, where γ_{IBM} the linear growth rate of IBM[22]. The radial grid width Δ_ψ is roughly estimated as $\Delta_\psi \simeq 1.2 \times 10^{-4} [R_{\mathrm{ax}}] (= 0.4 [\mathrm{mm}]) < \Delta_\eta < \Delta_\lambda$ so that the radial grid is fine enough to resolve the $n = 70$ mode.

IV. NONLINEAR SIMULATIONS

For nonlinear simulations, the same parameters as for linear calculations except $n_z = 128$ for the 1/5-th of torus are employed. A lowpass filter is set at the 32nd harmonics $n_{lp} = 32$ in the axisymmetric directions avoid aliasing error so that $n = 0, 5, \ldots, 160$ modes are taken into account. Here, the 32nd harmonic is a small enough number to satisfy the 2/3

dealiasing rule $n_{\text{alias}} = (128/2) \times (2/3) \sim 42$ and high-n modes are introduced as an energy sink for the nonlinear energy cascade during the pedestal collapse. The temporal resolution is $\Delta t = 1\,[t_A]$. Note that this is the output, not the internal time step, which is adaptive. The following multi-helicity perturbation with a truncated ballooning transformation is applied on the perturbed vorticity ϖ as an initial perturbation,

$$\varpi_{\text{init}} = \sum_{i=-3}^{3} \sum_{k=1}^{32} \varpi_{\text{init},k} \exp(-X^2) \exp(-Y^2) \sin(Z), \tag{12}$$
$$X = (x' - 0.5)/0.1, \quad Y = [y' - (i + 0.5)]/0.3, \quad Z = 2\pi k(z' + 5qi)$$

where $0 \leq x' \leq 1$, $0 \leq y' < 1$ and $0 \leq z' < 1$ are normalized coordinates corresponding to the field-aligned coordinates (See Appendix A 2), linear in grid index, and the initial amplitudes $\varpi_{\text{init},k}$ are small enough to resolve the linear phase growth.

A. Impact of $n = 0$ net flow and $n = 0$ magnetic field on energy loss

In the original BOUT++ code, CCs $\phi_{(m,0)}$ have been set to balance with the ion diamagnetic flow $\delta_i p_{(m,0)}$ without solving the $n = 0$ component of vorticity equation namely, the net flow is set to be zero $F_{(m,0)} = 0$, where $m = 0, 1, \cdots$. The $n = 0$ magnetic field is also assumed to be zero $A_{\parallel(m,0)} = 0$. For nonlinear simulations, solving the $(m \neq 0, 0)$ component of vorticity equation is important to obtain consistent $n = 0$ magnetic field evolution since the pedestal collapse gives a large deformation of zonal pressure, $p_{(0,0)}$ which is coupled with the toroidal curvature term in vorticity equation.

In some previous BOUT++ simulations, only ZFs $\phi_{(0,0)}$ were taken into account and the $(m \neq 0, 0)$ component of vorticity equation was filtered out. This scheme was applied to an electrostatic turbulence collapse simulation[36] and ELM crash simulations[24,25] including the effect of the geodesic acoustic mode (GAM)[37]. GAM is produced by the poloidal mode coupling between $\phi_{(0,0)}$ and $p_{(1,0)}$ so that solving only the $(0, 0)$ component of vorticity equation is enough for GAM physics. Even in this scheme, $A_{\parallel(m,0)} = 0$ was still assumed.

To investigate a generation mechanism of $F_{(m,0)}$ and $A_{\parallel(m,0)}$ driven by RBM turbulence and an interplay with CCs, we briefly show the impact of them on the energy loss by comparing a simulation without $n = 0$ net flow and magnetic field like previous BOUT++ works where CCs are evaluated from the relation $\phi_{(m,0)} = -\delta_i p_{(m,0)}$ and that with them.
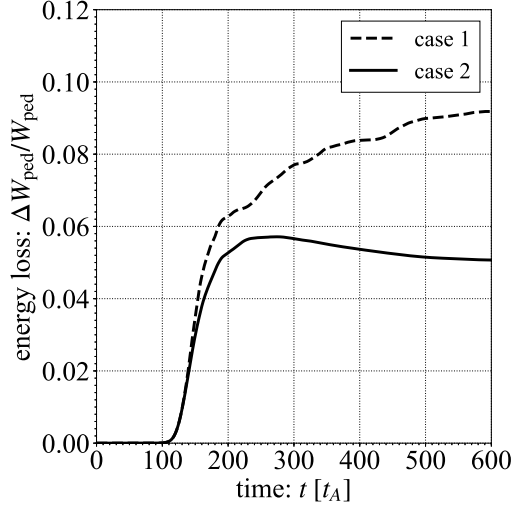
10

FIG. 3. Time evolution of plasma energy loss $\Delta W_{\mathrm{ped}}/W_{\mathrm{ped}}$ in case 1 (dashed) and that in case 2 (solid) from $t = 0$ $[t_A]$ to $t = 600$ $[t_A]$ in the nonlinear relaxation phase.

Here we will express these cases as case 1 with $F_{(m,0)} = 0$ and $A_{\parallel (m,0)} = 0$, and case 2 with $F_{(m,0)} \neq 0$ and $A_{\parallel (m,0)} \neq 0$ respectively.

The impact of $F_{(m,0)}$ and $A_{\parallel (m,0)}$ on the energy loss level $\Delta W_{\mathrm{ped}}/W_{\mathrm{ped}}$ is shown in Fig. 3. The energy loss level shows considerable difference in the nonlinear relaxation phase. This difference is caused mainly by differences in the $n = 0$ radial electric field shear and the $n = 0$ parallel current generated during the pedestal collapse. Time evolution of flux-surface averaged radial electric field $\langle E_r \rangle_S$, total pressure $\langle p \rangle_S = \langle p_0 + p_1 \rangle_S$, total parallel current $\langle J_\parallel \rangle_S = \langle J_{\parallel 0} + J_{\parallel 1} \rangle_S$ and ion parallel flow $\langle v_\parallel \rangle_S$ and poloidal slices of perturbed component of those quantities E_{r1}, p_1, $J_{\parallel 1}$ and $v_{\parallel 1}$, after the pedestal collapse $t = 600$ $[t_A]$ are shown in Fig. 4. Here, $\langle f \rangle_S = \int_S f J d\theta d\zeta / \int_S J d\theta d\zeta$ represents the quantity f averaged over the flux surface, where (ψ, θ, ζ) is the flux coordinate system (See Appendix A 1).

It is seen that the $\langle E_r \rangle_S$ profile in case 2 is sheared more strongly in the radial direction than that of case 1. E_r shear breaks pressure filaments into pieces. As the result, inward and outward radial transport of pressure filaments is suppressed and a reduction of energy loss level is attained, which is consistent with results from Refs. 13, 15, and 18. Here, $\langle E_r \rangle_S = 2.1 \times 10^{-3}$ $[B_{\mathrm{ax}} V_A]$ is about 41 $[\mathrm{kV/m}]$ in SI units since the radial electric field is normalized with $B_{\mathrm{ax}} V_A = 1.95 \times 10^7$ $[\mathrm{V/m}]$.

For the parallel current profile, $\langle J_\parallel \rangle_S$ collapses at around the pressure peak $\psi \simeq 0.856$
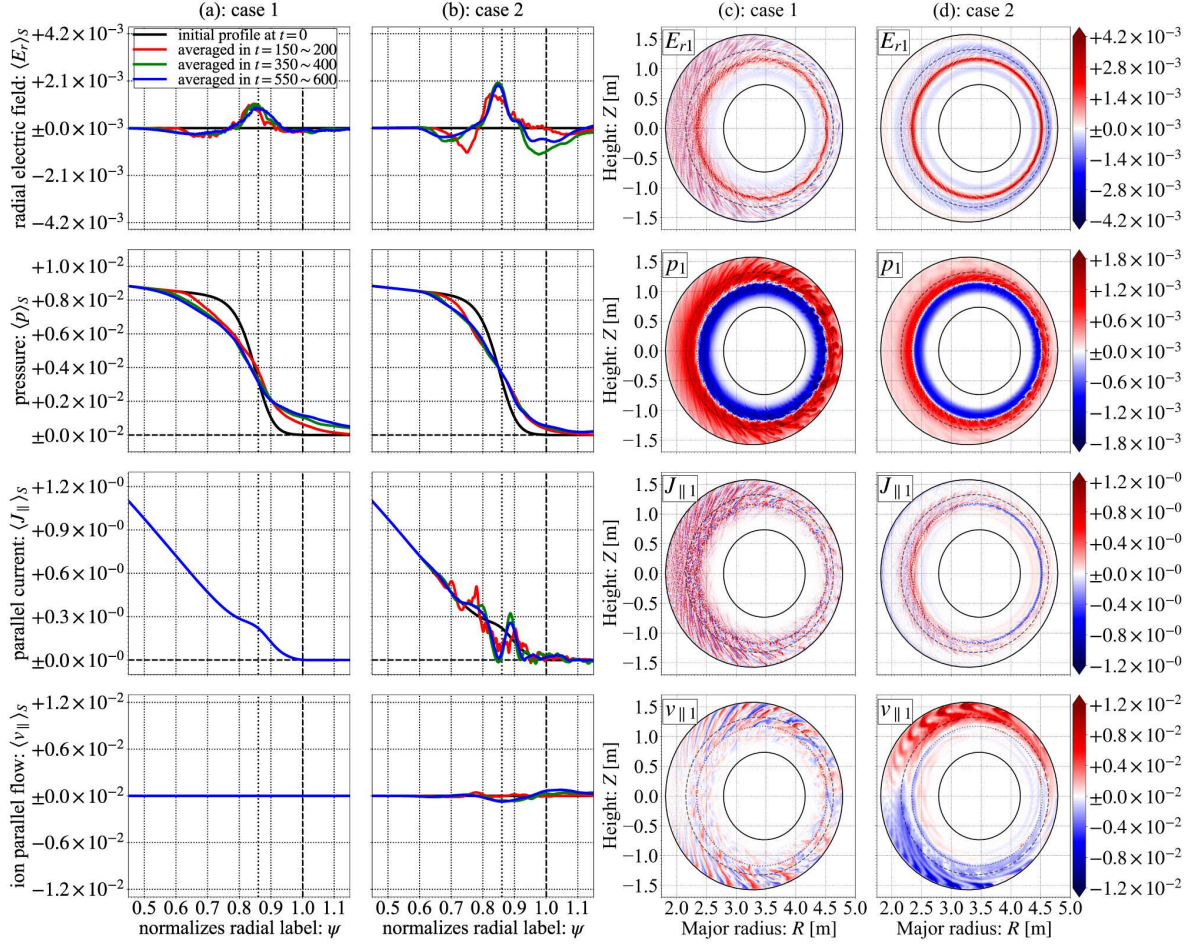
FIG. 4. (a) time evolution of flux-surface averaged radial profile of radial electric field $\langle E_r \rangle_S$ $[B_{ax} V_A]$, total pressure $\langle p \rangle_S$ $[B_{ax}^2/2\mu_0]$, total parallel current $\langle J_\parallel \rangle_S$ $[-B_{ax}/\mu_0 R_{ax}]$, and ion parallel flow $\langle v_\parallel \rangle_S$ $[V_A]$ in case 1, (b) those in case 2, (c) poloidal slices of perturbed part of those quantities after the crash $t = 600$ $[t_A]$ in case 1 and (d) those in case 2 respectively. The color bars to the right are in normalized units.

indicated by the dotted lines in case 2, while only fine filament structures appear on the poloidal slice in case 1. The global $(m \neq 0, 0)$ structure as well as the fine filament structure also appear on the poloidal slice of perturbed parallel current $J_{\parallel 1}$ in case 2.

For the ion parallel flow in case 2, the global $(m \neq 0, 0)$ structure as well as the fine filament structure appear on the poloidal slice of perturbed ion parallel flow $v_{i\parallel}$ while $\langle v_\parallel \rangle_S$ is not strongly generated compared to $v_{\parallel (m \neq 0, 0)}$.

These results show that solving the $n = 0$ components of vorticity equation and Ohms law has a significant impact on the result, both quantitatively and qualitatively.

B. Generation mechanism of $n = 0$ net flow and magnetic field

In this subsection, the generation mechanism of $F_{(m,0)}$ and $A_{\parallel(m,0)}$ is investigated. Here-after all figures show results in the case 2 with $F_{(m,0)} \neq 0$ and $A_{\parallel(m,0)} \neq 0$.

The time evolution of system energies: internal energy W_p, perpendicular kinetic energy W_k, magnetic energy W_m, parallel kinetic energy W_v and energy loss level $\Delta W_{\mathrm{ped}}/W_{\mathrm{ped}}$ is shown in Fig. 5, where each energy includes all toroidal modes given by $W_p = \sum_{i=0}^{32} W_p^{n=5i}$. The internal energy is larger than the other energies by $\mathcal{O}(10^{4 \sim 5})$ after the pedestal collapse and saturates at $t = 2000 \ [t_A]$.

For the other energies, the parallel kinetic energy monotonically decreases after the pedestal collapse. It only weakly couples with the other perturbed variables via the ion parallel flow compression terms in the energy equation Eq. (2) and has little impact on perpendicular flow and magnetic field. The magnetic energy is larger than the perpendicular kinetic energy in the nonlinear relaxation phase, which means that RBM turbulence is electromagnetic in nature rather than electrostatic.

The time evolution of energy loss level (white curve) and power spectrum of perpendicular kinetic energy over the entire simulated time are summarized in Fig. 5(b). Linearly unstable modes with $n = 20 \sim 60$ grow in the linear phase $t < 120 \ [t_A]$ and the energy cascade from the linearly unstable modes to their higher harmonics and inverse energy cascade to CCs occur during the pedestal collapse phase $120 \ [t_A] < t < 240 \ [t_A]$. The energy loss level decreases in $t > 240 \ [t_A]$ and then increases again due to the secondary instability at $t = 825 \ [t_A]$. A strong energy cascade occurs at $t \sim 800 \ [t_A]$ prior to the secondary collapse. A secondary instability develops in the range of toroidal Fourier modes with $n = 15 \sim 40$ after $t = 400 \ [t_A]$ and results in the monotonic increase of energy loss level after the secondary collapse.

The time evolution of each toroidal Fourier harmonic of internal energy and that of perpendicular kinetic energy are summarized in Fig. 6, where the black solid curves indicate total energy in Fig. 5(a). Figure 6(a) indicates that $n = 0$ internal energy decreases after the pedestal collapse and then increases again due to the excitation of a secondary instability around $t = 400 \ [t_A]$. The peak in mode amplitude is located at $n \leq 30$ and $n = 20$ is the largest one during the secondary collapse around $t = 800 \ [t_A]$. After the secondary collapse, the $n = 20$ mode damps and then other modes are excited. This secondary instability could
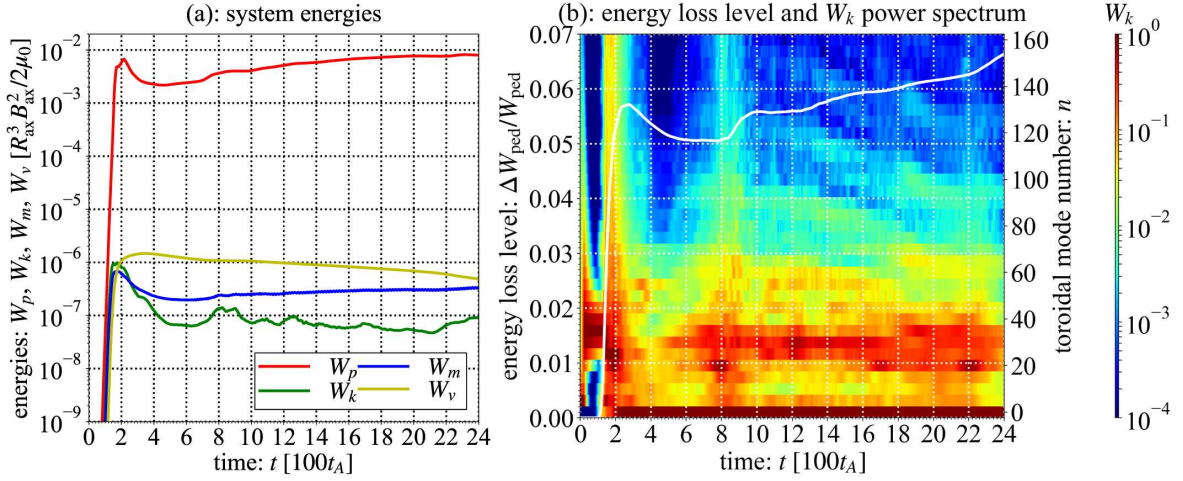
13

FIG. 5. Time evolution of (a) system energies including internal energy W_p (red), kinetic energy of perpendicular flow W_k (green), magnetic energy W_m (blue) and kinetic energy of parallel flow W_v (yellow) and (b) energy loss level $\Delta W_{\rm ped}/W_{\rm ped}$ (white solid) and toroidal mode spectrum of perpendicular kinetic energy W_k (color map). Here the toroidal mode spectrum of W_k has been normalized to set the maximum mode of W_k unity at every time step.

be the Kelvin-Helmholtz instability quasi-linearly excited by CCs after the pedestal collapse but further analyses are necessary to identify the instability.

The peak in mode amplitude after $t = 400\,[t_A]$ is more clearly seen in the power spectrum of the perpendicular kinetic energy in Fig. 6(b). The peak in mode amplitude with $n = 20$ becomes comparable to that of CCs during the secondary collapse. The generation mechanism of $F_{(m,0)}$ and $A_{\parallel(m,0)}$ are investigated by energy transfer rate analyses on $n = 0$ component of internal energy and perpendicular kinetic energy.

Figure 7 shows the time evolution of $n = 0$ internal energy transfer rate. It is found that the main contribution comes from $E \times B$ convection and diffusion terms while the contribution from flow compression effects is negligibly small compared to the other contributions. This is because the flux-surface averaged pressure $\langle p \rangle_S$ is strongly deformed by the pedestal collapse as shown in Fig. 4(b) and Fig. 4(d).

After the crash $t \geq 120\,[t_A]$, the line-bending term $T_{k,LB}^{(m,0)}$ is strongly generated to balance with the toroidal curvature term $T_{k,C}^{(m,0)}$ while the kink term $T_{k,K}^{(m,0)}$ and the Maxwell stress term $T_{k,M}^{(m,0)}$ are negligibly small compared to the line-bending term. $J_{\parallel(m\neq0,0)}$ is strongly generated, which is also seen at the poloidal slice of the perturbed parallel current in Fig. 4(d).
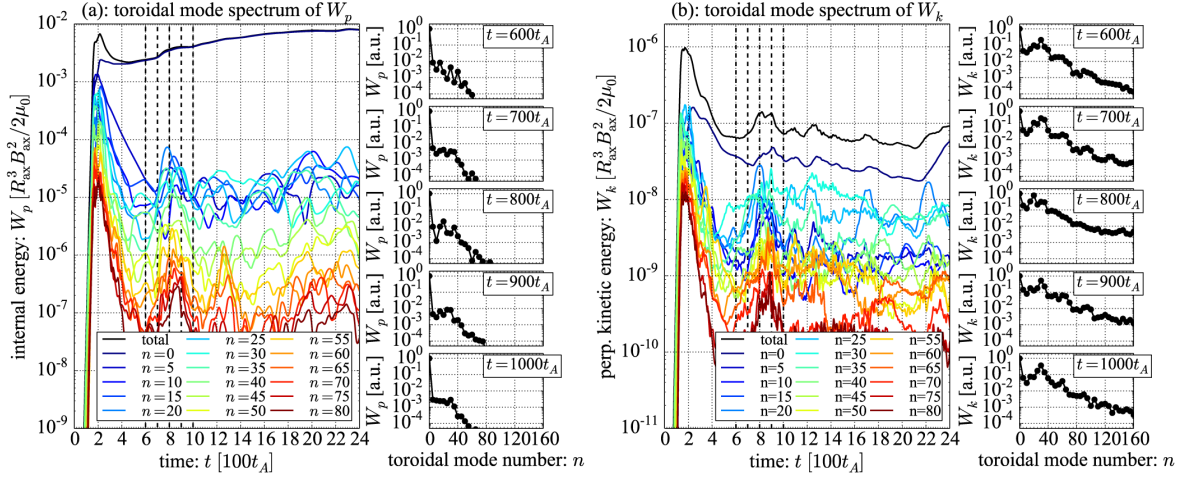
14

FIG. 6. Time evolution and five time slices during the secondary collapse $t \sim 800$ $[t_A]$ of toroidal mode spectrum of (a) internal energy W_p and (b) perpendicular kinetic energy W_k respectively. In the time evolution of toroidal mode spectrum W_p and W_k, the toroidal modes up to $n = 80$ are plotted for comparison and each time of slices are indicated by the black dashed lines.
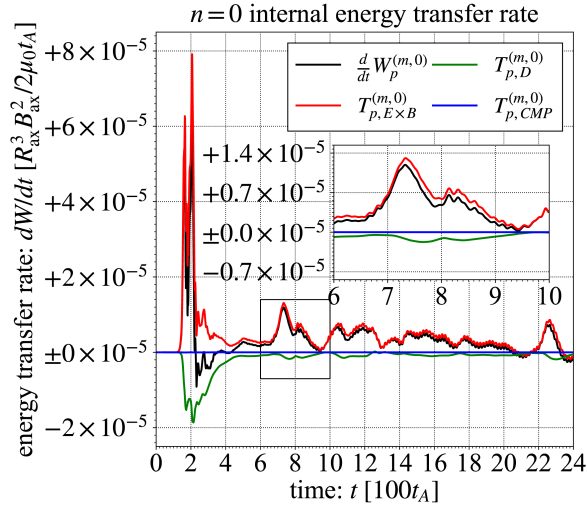

FIG. 7. Time evolution of energy transfer rates by the terms in equation of internal energy to $n = 0$ internal energy transfer rate.

It should be noted that solving the $(m \neq 0, 0)$ component of the vorticity equation, to ensure force balance, requires the two-dimensional Poisson solver for CCs in the BOUT++ framework.

Figure 8(b) shows the time evolution of the residual of force balance among the $\boldsymbol{J} \times \boldsymbol{B}$
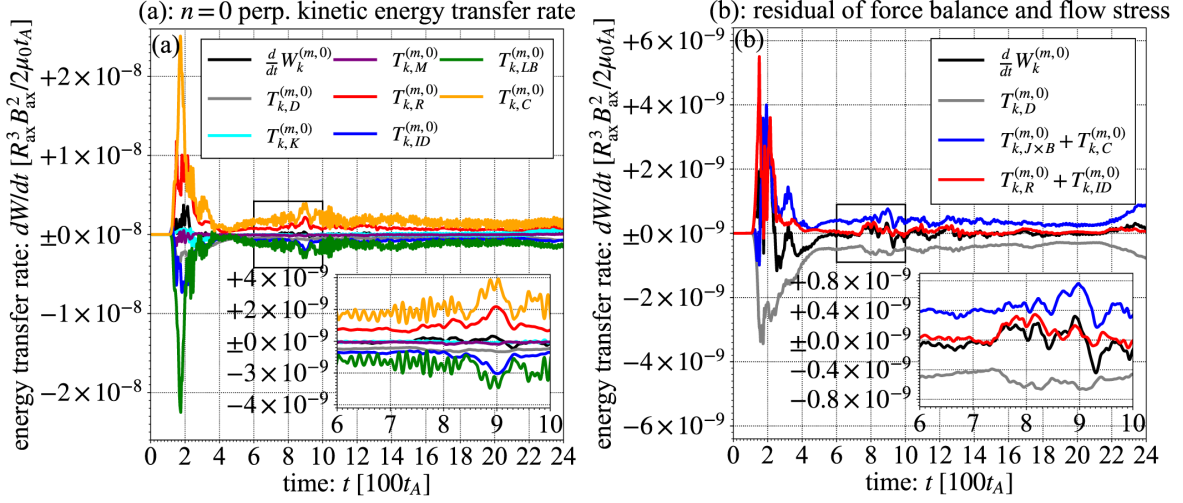
15

FIG. 8. Time evolution of (a) energy transfer rates by the terms in equation of perpendicular kinetic energy to $n = 0$ perpendicular kinetic energy transfer rate and (b) energy transfer rates by residual of flow stress $T_{k,R}^{(m,0)} + T_{k,ID}^{(m,0)}$, by residual of force balance $T_{k,J \times B}^{(m,0)} + T_{k,C}^{(m,0)}$ and by dissipation $T_{k,D}^{(m,0)}$.

force $T_{k,J \times B}^{(m,0)}$, pressure gradient $T_{k,C}^{(m,0)}$ and dissipation $T_{k,D}^{(m,0)}$ as well as the residual of flow stress including the Reynolds stress $T_{k,R}^{(m,0)}$ and the ion diamagnetic flow stress $T_{k,ID}^{(m,0)}$. It is found that the residual of force balance is almost canceled out by dissipation. To identify the generation mechanism of CCs in this simulation, we create two groups: the local interaction by doublet of fluctuation quantities and non-local interaction by triplet of them in Eq. (10). Figure 9 shows the time evolution of energy transfer rate of this categorization. It is shown that the non-local interaction via Reynolds stress, ion diamagnetic flow stress, and Maxwell stress can also produce CCs (See Fig 4) via the secondary instability just before the secondary collapse $700\,[t_A] < t < 800\,[t_A]$ while the local interaction produces them after the secondary collapse $800\,[t_A] < t$, where middle-n modes are smeared out.

C. Interplay between CCs and RBM turbulence after secondary collapse

The analyses in the previous subsection show the generation mechanism of $F_{(m,0)}$ and $A_{\parallel(m,0)}$ by a secondary instability. However, spatial structures are not yet clarified. In this subsection, we investigate spatio-temporal structures of flux-surface averaged pressure
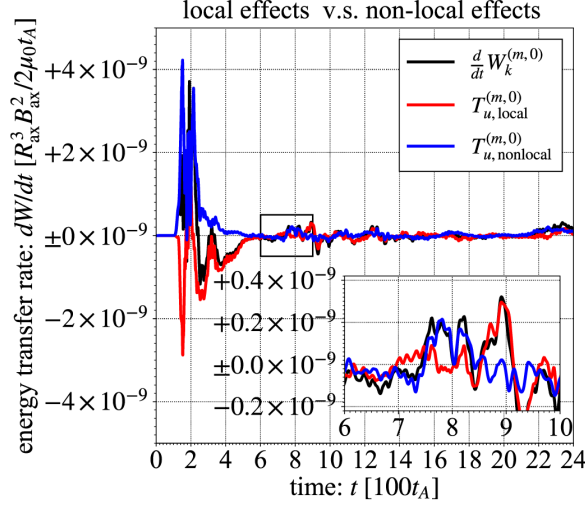
16

FIG. 9. Time evolution of energy transfer rates to $n = 0$ perpendicular kinetic energy by local effects $T_{k,\text{local}}^{(m,0)}$ (red) and that by non-local effects $T_{k,\text{nonlocal}}^{(m,0)}$ (blue)

gradient $\langle -\partial_r p \rangle_S$, $(1,0)$ component of parallel current at the outboard mid-plane $J_{\parallel(1,0)}$, $E \times B$ shearing rate[38,39] $\omega_{E \times B} = \langle (R^2 B_{\text{p0}}^2/B_0)\partial_\psi (E_r/B_{\text{p0}}R) \rangle_S$ and turbulence intensity $\mathcal{S} = \sqrt{\sum_{m'} \sum_{n' \neq 0} \phi_{(m',n')}\phi_{(-m',-n')}}$ and the phase diagram among them to investigate nonlinear dynamics. $J_{\parallel(1,0)}$ is evaluated in the straight field-line coordinate system (ψ, ϑ, ζ) by using the relation $\vartheta(\psi, \theta) = q^{-1} \int^\theta (B^\zeta/B^\theta)d\theta$

The spatio-temporal structures of these quantities in Fig. 10 describe the physical picture of energy loss processes in the pedestal collapse. Radial profiles of the pressure gradient and the parallel current spread radially from their initial peak positions at the beginning of the pedestal collapse $t = 120$ $[t_A]$ and then partially return to their initial peak positions after which the $\boldsymbol{J} \times \boldsymbol{B}$ force balances with the pressure gradient with the small residual as is shown in Fig. 8, resulting in a decrease of energy loss level after $t = 240$ $[t_A]$. On the other hand, the residual of force balance generates two strong flow shear regions beside the initial pressure gradient peak position, while there is the thin weak flow shear layer between them. This strong flow shear locks pressure gradient fronts and parallel current fronts at the outside of the flow shear region so that the energy loss level transiently saturates by the secondary collapse $t = 825$ $[t_A]$.

A damped oscillation with long period $\tau = 100 \sim 300$ $[t_A]$ $(= 7 \sim 21$ $[\text{kHz}])$ spreading radially from around $0.95 \leq \psi \leq 1$ appears after the pedestal collapse and continues to the
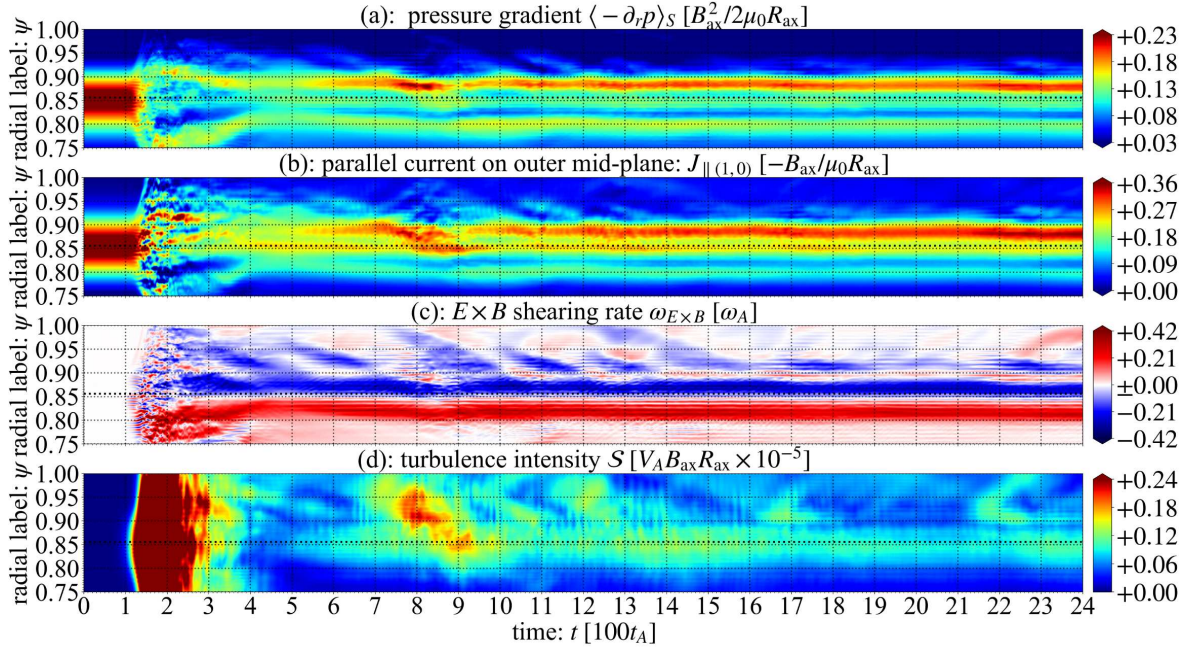
17

FIG. 10. Spatio-temporal structure of (a) flux-surface averaged pressure gradient $\langle -\partial_r p \rangle_S$, (b) $(1,0)$ component of parallel current on the outboard mid-plane $J_{\parallel (1,0)}$, (c) $E \times B$ shearing rate $\omega_{E \times B}$, and (d) turbulence intensity $\mathcal{S}$ respectively, where the thick dotted lines represent the pressure gradient peak position and the color maps are scaled to emphasize the structures after $t = 600$ $[t_A]$.

secondary collapse as is shown in Fig. 11. In $0.90 \leq \psi \leq 0.92$, pressure gradient gradually steepens in 650 $[t_A] \leq t \leq 750$ $[t_A]$ and then the local flow shear intensity weakens with delay. Turbulence with streamer structure is then excited and enhances non-local transport of pressure in $\psi \geq 0.88$. As a result, the pressure gradient around $\psi = 0.88$ steepens. This steep pressure gradient weakens the flow shear intensity around $\psi = 0.88$ at $t = 825$ $[t_A]$ so that the streamer penetrates to the inner region and the pressure gradient $\psi = 0.88$ is finally flattened by the non-local transport caused by the streamer. After the secondary collapse, the amplitude of damped oscillations reduces in the inner region due to the absence of heat source and disappears after $t = 1400$ $[t_A]$, while RBM turbulence in $0.8 \leq \psi \leq 0.9$ enhances radial energy transport resulting in the monotonic increase of energy loss level.

It is clearly observed in Fig. 10(c) that the flow shear intensity in $0.88 \leq \psi \leq 1.0$ changes temporally in accordance with the damped oscillation while that in $\psi \leq 0.88$ is almost constant after the secondary collapse. To identify a negative feed back loop for the
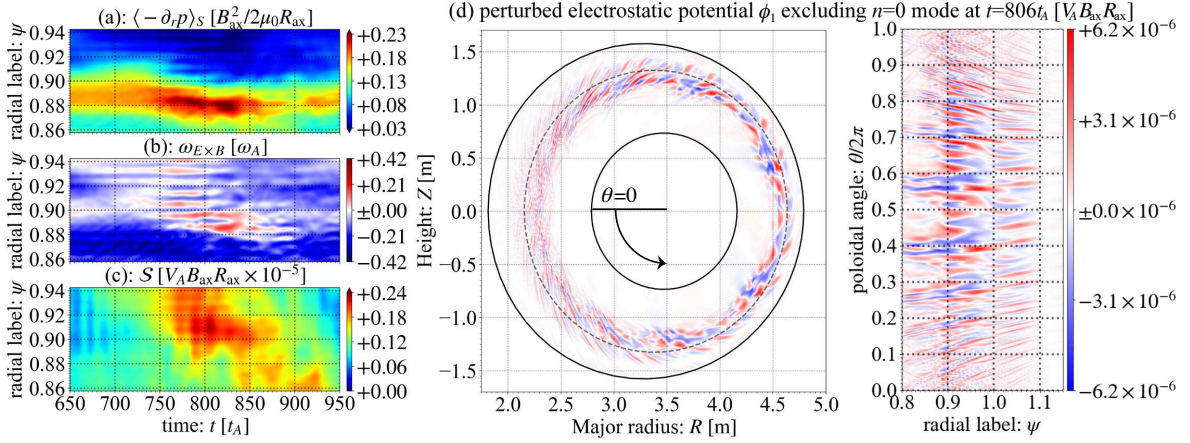
18

FIG. 11. Spatio-temporal structure of (a) flux-averaged pressure gradient $\langle -\partial_r p \rangle_S$, (b) $E \times B$ shearing rate $\omega_{E \times B}$ and (c) turbulence intensity $\mathcal{S}$ during the secondary collapse. (d) perturbed electrostatic potential ϕ_1 excluding CCs at $t = 806$ $[t_A]$ which shows the streamer structure enhancing the non-local radial transport.

damped oscillation, the phase diagram among pressure gradient $\langle -\partial_r p \rangle_S$, parallel current $J_{\parallel(1,0)}$, $E \times B$ shearing rate $\omega_{E \times B}$ and turbulence intensity $\mathcal{S}$ averaged in $0.91 \leq \psi \leq 0.92$ is investigated.

Figure 12(a) shows that the parallel current simultaneously changes in accordance with pressure gradient. The Lissajous diagram between them therefore becomes a damped reciprocal orbit as is shown in Fig. 12(b). The parallel current responds such that the line-bending term balances the curvature term to suppress CCs generation after the secondary collapse phase.

Figure 12(c) shows that the pressure gradient changes prior to the $E \times B$ shearing rate and the Lissajous diagram between them is a damped elliptical orbit. Finally Fig. 12(e) shows that the pressure gradient also responds prior to the turbulence intensity and the Lissajous diagram between them is a damped elliptical orbit as in Fig. 12(f). Since the turbulence is generated by the free energy of pressure gradient and the increase of turbulence transport reduces the pressure gradient, this negative feed back loop drives the damped oscillation. The damped oscillation is therefore a pressure driven oscillation[40] in which the pressure gradient is the prey and the turbulence is the predator rather than the turbulence driven oscillation[41] where the turbulence is the prey and the ZFs are the predator.
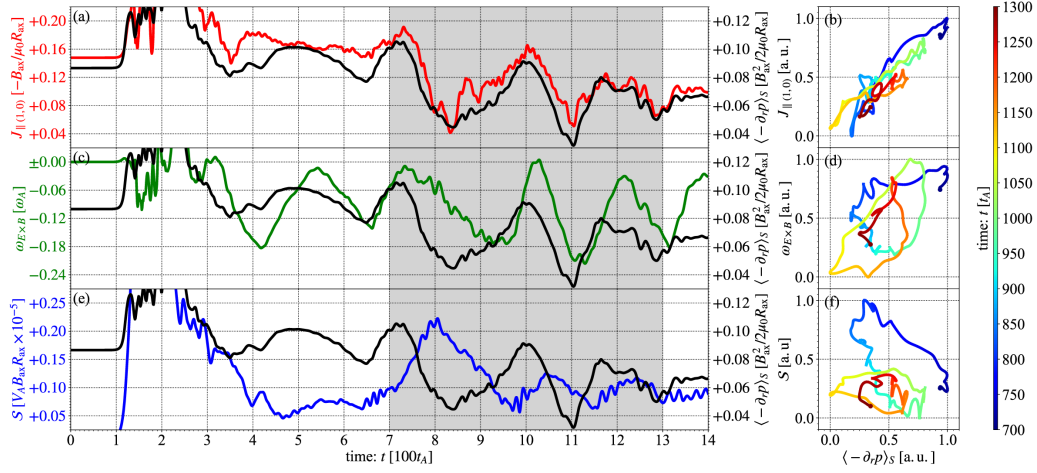
19

FIG. 12. (a) time evolution of $J_{\|(1,0)}$ (red) and $\langle -\partial_r p \rangle_S$ (black), (b) Lissajous diagram between $J_{\|(1,0)}$ and $\langle -\partial_r p \rangle_S$, (c) time evolution of $\omega_{E \times B}$ (green) and $\langle -\partial_r p \rangle_S$ (black), (d) Lissajous diagram between $\omega_{E \times B}$ and $\langle -\partial_r p \rangle_S$ (e) time evolution of $\mathcal{S}$ (blue) and $\langle -\partial_r p \rangle_S$ (black), and (f) Lissajous diagram between $\mathcal{S}$ and $\langle -\partial_r p \rangle_S$ respectively, where the physical quantities are averaged in $0.91 \leq \psi \leq 0.92$ and the color map represents the time evolution from $t = 700$ $[t_A]$ (blue) to $t = 1300$ $[t_A]$ (red).

V. SUMMARY

In summary, the generation mechanism of $n = 0$ net flows $F_{(m,0)}$ and magnetic field $A_{\|(m,0)}$ after the pedestal collapse and the interplay between CCs and RBM turbulence after the secondary collapse have been studied by using a four-field reduced MHD model and shifted circular equilibrium in the BOUT++ framework including the two-dimensional Poisson solver for CCs.

The simulation in the case with $F_{(m,0)} \neq 0$ and $A_{\|(m,0)} \neq 0$ has shown that CCs suppress radial propagation of pressure filaments like Refs.13, 15, and 18 and the pressure pedestal recovers partially after the pedestal collapse. These effects result in the considerable reduction of energy loss level compared to the case with $F_{(m,0)} = 0$ and $A_{\|(m,0)} = 0$ as was used in previous BOUT++ simulations. These results show that solving the $n = 0$ components of vorticity equation and Ohms law has a significant impact on the result, both quantitatively and qualitatively.

According to the energy transfer rate analyses of $n = 0$ system energies, it has been

20

shown that $n = 0$ net flow is generated by the residual of force balance described by the $(m \neq 0, 0)$ component of the vorticity equation before a secondary collapse. It is found that the contribution from the residual of flow stress to $n = 0$ net flow becomes comparable with that of force balance during the secondary collapse. In particular, just before the secondary collapse, the secondary instability drives CCs via the non-local interaction.

The time evolution of toroidal mode spectrum of internal energy and perpendicular kinetic energy shows that $n = 0$ internal energy decreases after the pedestal collapse and then increases due to the secondary instability, where the peak is located in $n \leq 30$. The secondary collapse at $t = 800$ $[t_A]$ results in the rapid increase of energy loss level. It can increase the energy loss level released by a single collapse event. This secondary instability could be the Kelvin-Helmholtz instability quasi-linearly driven by CCs after the pedestal collapse but further analyses are required to identify it, which is left as a future work.

The spatio-temporal analyses have revealed that the strong flow shear generated after the pedestal collapse locks the pressure and parallel current profile at the outside of the flow shear regions while the secondary collapse occurs via the non-local transport enhanced by streamer. The phase diagram analyses have also shown that the damped oscillation is driven by the pressure-driven negative feedback loop between pressure gradient and turbulence, where the prey is the pressure gradient and the predator is the turbulence.

ACKNOWLEDGMENTS

Appendix A: Coordinate systems for tokamak edge simulations in BOUT++

The quasi-ballooning coordinate system is a non-commutative right-handed system consisting of a radial coordinate label defined in an orthogonal flux coordinate system[42] and a parallel coordinate label defined in the field-aligned coordinate system. The last coordinate label can be either a toroidal label in the orthogonal coordinate system or a binormal label in the field-aligned coordinate system. In this section, we describe relations among these coordinate systems, which helps readers to understand the tokamak coordinate system in BOUT++ reported in Ref. 20.

1. Orthogonal flux coordinate system

The orthogonal flux coordinate system (ψ, θ, ζ) is a kind of flux coordinate systems, the poloidal angle label θ of which is designed to be orthogonal to the other directions, where ψ is the poloidal magnetic flux function used as the radial label and ζ is the geometrical toroidal angle respectively. In this system, the equilibrium magnetic field $\boldsymbol{B}$ can be expressed as

$$\boldsymbol{B} = B^\theta \boldsymbol{e}_\theta + B^\zeta \boldsymbol{e}_\zeta = B_\theta \boldsymbol{e}^\theta + B_\zeta \boldsymbol{e}^\zeta = B_\mathrm{p} \hat{\boldsymbol{e}}_\theta + B_\mathrm{t} \hat{\boldsymbol{e}}_\zeta, \tag{A1}$$

where $\boldsymbol{e}_{x_i} = \partial \boldsymbol{R}/\partial x_i$ are tangential basis vectors, $\boldsymbol{e}^{x_i} = \nabla x_i$ are reciprocal basis vectors, $\hat{\boldsymbol{e}}_{x_i} = h_{x_i} \boldsymbol{e}^{x_i} = h_{x_i}^{-1} \boldsymbol{e}_{x_i}$ are unit basis vectors for $x_i = (\psi, \theta, \zeta)$, B_p is the poloidal magnetic field and B_t is the toroidal magnetic field respectively. The covariant metric tensor becomes diagonal as

$$g_{\psi\psi} = h_\psi^2 = 1/B_\mathrm{p}^2 R^2, \quad g_{\theta\theta} = h_\theta^2, \quad g_{\zeta\zeta} = h_\zeta^2 = R^2, J = h_\psi h_\theta h_\zeta = \frac{h_\theta}{B_\mathrm{p}}, \tag{A2}$$

where R is the major radius and $h_\theta = |\boldsymbol{e}_\theta|$ is the poloidal arc length and the contravariant metric coefficients are also written as $g^{x_i x_i} = g_{x_i x_i}^{-1}$ due to its orthogonal property.

Since the orthogonal flux coordinate system is not a straight field line coordinate system, the local field line pitch defined by

$$\nu(\psi, \theta) = \frac{\boldsymbol{B} \cdot \nabla\zeta}{\boldsymbol{B} \cdot \nabla\theta} = \frac{B^\zeta}{B^\theta} = \frac{B_\mathrm{t} h_\theta}{B_\mathrm{p} R} \tag{A3}$$

can vary on the flux surface labeled with the radial label ψ. The safety factor q is therefore defined with a line integral of the local pitch over the poloidal direction

$$q = \frac{1}{2\pi} \oint \nu d\theta. \tag{A4}$$

22

For edge plasma simulations inside the LCFS, BOUT++ employs an annular torus domain divided into toroidally axisymmetric N parts defined with $\psi_{\text{in}} \leq \psi \leq \psi_{\text{out}}$, $0 \leq \theta \leq 2\pi$ and $0 \leq \zeta \leq 2\pi/N$ so that a bi-periodic boundary condition inside the LCFS can be written as

$$f(\psi, \theta + 2\pi, \zeta) = f(\psi, \theta, \zeta), \quad f(\psi, \theta, \zeta + 2\pi/N) = f(\psi, \theta, \zeta), \tag{A5}$$

where the outer mid-plane is given at $\theta = \pi$ in this paper.

2. Field-aligned coordinates: (x, y, z)

In BOUT++, the field-aligned coordinate system (x, y, z) defined by

$$x = \psi - \psi_o, \quad y = \theta, \quad z = \zeta - \alpha, \quad \alpha = \int_{\theta_o}^{\theta} \nu(\psi, \theta) d\theta \tag{A6}$$

is also used to efficiently simulate short wave-length instabilities, where ψ_o is the offset of the radial label, α is the shift angle designed to be $\alpha = 0$ at θ_o. In this paper, we set $\psi_o = \psi_{\text{sep}}$ and $\theta_o = \pi$, where the subscript sep represents a value at the separatrix.

The tangential basis vectors and the reciprocal basis vectors of the field-aligned coordinate system are expressed with those of the orthogonal flux coordinate system as

$$\boldsymbol{e}_x = \boldsymbol{e}_\psi + I\boldsymbol{e}_\zeta, \quad \boldsymbol{e}_y = \boldsymbol{e}_\theta + \nu\boldsymbol{e}_\zeta, \quad \boldsymbol{e}_z = \boldsymbol{e}_\zeta, \tag{A7}$$

$$\boldsymbol{e}^x = \boldsymbol{e}^\psi, \quad \boldsymbol{e}^y = \boldsymbol{e}^\theta, \quad \boldsymbol{e}^z = \boldsymbol{e}^\zeta - I\boldsymbol{e}^\psi - \nu\boldsymbol{e}^\theta, \tag{A8}$$

where

$$I = \int_{\theta_o}^{\theta} \frac{\partial \nu}{\partial \psi} d\theta \tag{A9}$$

is the quantity related to integrated local magnetic shear. With a straight field-line coordinate system (ψ, χ, ζ) with the poloidal angle $\chi(\psi, \theta) = q^{-1} \int \nu d\theta$, Eq. (A8) can be expressed as $I = q'(\chi - \chi_o)$, where $'$ represents ψ-derivative and $\chi_o = \chi(\psi, \theta_o)$. One can easily find from Eq. (A7) that the Jacobian of the field-aligned coordinate system also becomes $J = h_\theta/B_{\text{p}}$. The contravariant metric coefficient $g^{x_i x_j}$ and the covariant metric coefficient $g_{x_i x_j}$ in the field-aligned coordinate system for $(x_i, x_j) = (x, y, z)$ are also straightforwardly derived from

23

Eq. (A2) and Eq. (A3) as

$$g_{x_i x_j} = \boldsymbol{e}_{x_i} \cdot \boldsymbol{e}_{x_j} = \begin{pmatrix} g_{\psi\psi} + I^2 g_{\zeta\zeta} & \nu I g_{\zeta\zeta} & I g_{\zeta\zeta} \\ \nu I g_{\zeta\zeta} & g_{\theta\theta} + \nu^2 g_{\zeta\zeta} & \nu g_{\zeta\zeta} \\ I g_{\zeta\zeta} & \nu g_{\zeta\zeta} & g_{\zeta\zeta} \end{pmatrix}, \tag{A10}$$

$$g^{x_i x_j} = \boldsymbol{e}^{x_i} \cdot \boldsymbol{e}^{x_j} = \begin{pmatrix} g^{\psi\psi} & 0 & -I g^{\psi\psi} \\ 0 & g^{\theta\theta} & -\nu g^{\theta\theta} \\ -I g^{\psi\psi} & -\nu g^{\theta\theta} & I^2 g^{\psi\psi} + \nu^2 g^{\theta\theta} + g^{\zeta\zeta} \end{pmatrix}. \tag{A11}$$

In the field-aligned coordinates, the equilibrium magnetic field $\boldsymbol{B}$ can be written in Clebsch form

$$\boldsymbol{B} = \boldsymbol{e}^z \times \boldsymbol{e}^x = \frac{\boldsymbol{e}_y}{J} \tag{A12}$$

so that the differentials along the field line can be expressed with only the parallel label y

$$\boldsymbol{b} \cdot \nabla = \frac{1}{JB} \frac{\partial}{\partial y} = \frac{1}{\sqrt{g_{yy}}} \frac{\partial}{\partial y}. \tag{A13}$$

This fact means that the grid resolution in the y direction can be reduced for $k_\perp / k_\parallel \ll 1$. The left of Fig. 13 shows that the numerical grid defined in the field-aligned coordinate system is aligned to magnetic field lines.

While the field-aligned coordinate system can reduce computational cost for parallel derivatives, I gives a secular parallel cell deformation degrading numerical accuracy of x-derivatives as is shown in the center and the right of Fig. 13. Although there is no cell deformation on $y = \pi$-surface due to the absence of the shifted angle $\alpha = 0$, the grid is strongly deformed in the toroidal direction on $y = 0$-surface with $\alpha = \pi$.

To remedy this problem, BOUT++ employs the shifted radial derivative method[43,44] obtained from the chain rule of differential Eq. (A7)

$$\frac{\partial f}{\partial x} = \boldsymbol{e}_x \cdot \nabla f = (\boldsymbol{e}_\psi + I \boldsymbol{e}_\zeta) \cdot \nabla f = \frac{\partial f}{\partial \psi} + I \frac{\partial f}{\partial \zeta}. \tag{A14}$$

The coordinate transform between the field-aligned coordinate system and the orthogonal flux coordinate system required for ψ-derivative can be done with a discrete Fourier transform $\mathcal{F}$ and an inverse discrete Fourier transform $\mathcal{F}^{-1}$ in either ζ-direction or z-direction,

$$f(\psi, \theta, \zeta) = \mathcal{F}^{-1} \left\{ \mathcal{F} \left\{ f(x, y, z) \right\} e^{-ikN\alpha} \right\} = \mathcal{F}^{-1} \left\{ F(\psi, \theta, n) \right\}, \tag{A15}$$

$$f(x, y, z) = \mathcal{F}^{-1} \left\{ \mathcal{F} \left\{ f(\psi, \theta, \zeta) \right\} e^{ikN\alpha} \right\} = \mathcal{F}^{-1} \left\{ F(x, y, n) \right\}, \tag{A16}$$
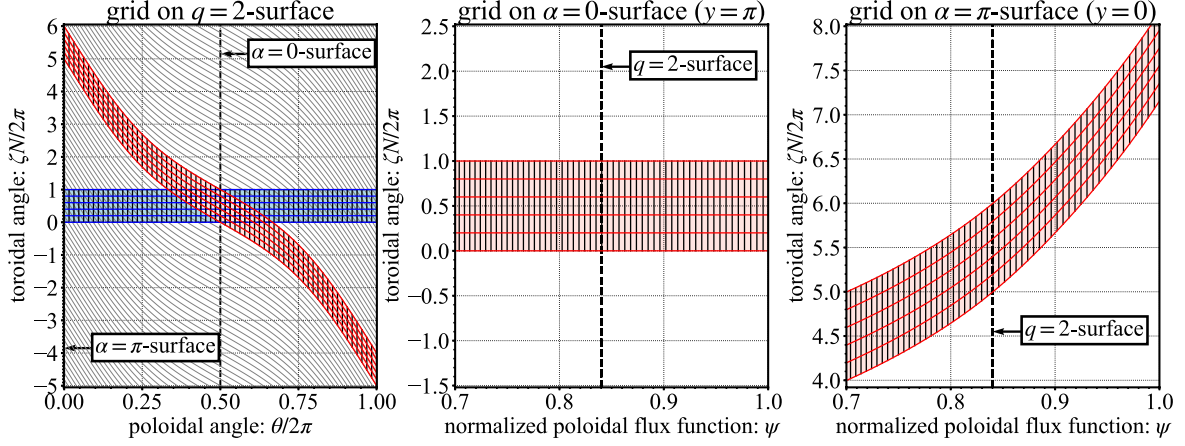
FIG. 13. A rectangular grid constructed in the field-aligned coordinate system expressed in the orthogonal flux coordinate system for $N = 5$: the field-aligned grid (red), an orthogonal flux grid (blue) and magnetic field-lines (gray) on $q = 2$-surface (left), the field-aligned grid in the edge region on $\alpha = 0$-surface (or $y = \pi$-surface) (center) and the field-aligned grid in the edge region on $\alpha = \pi$-surface (or $y = 0$-surface) (right) respectively. These figures are constructed from the shifted circular equilibrium shown in Fig. 1 where the safety factor q is negatively defined. In this paper, $-q$ is employed for figures instead of q for readability

where i is the imaginary unit, k is the mode number in the axisymmetric directions in the $1/N$-th annular toroidal wedge and $n = kN$ is the effective toroidal mode number in the annular torus respectively. The bi-periodic boundary condition inside the LCFS Eq. (A5) also becomes the following twisted bi-periodic boundary condition in the field-aligned coordinate system

$$f(x, y + 2\pi, z - 2\pi q) = f(x, y, z), \quad f(x, y, z + 2\pi/N) = f(x, y, z), \quad \text{(A17)}$$

which is applied on perturbed fields in the Fourier space with machine precision accuracy. The basic idea of the field-aligned coordinate system with shifted radial derivative used in BOUT and BOUT++ is reviewed in Refs. 8 and 9.

3. Quasi-ballooning coordinate system

The metric coefficients of the field-aligned coordinate system Eq. (A10) and Eq. (A11) and the radial derivative ∂_x evaluated with the shifted radial derivative Eq. (A14) still have

I which degrades the numerical accuracy of simulations. BOUT++ therefore has another coordinate system named the quasi-ballooning coordinate system where the metrics and basis vectors are complicated but can be expressed without I.

The quasi-ballooning coordinate system is a combination of the orthogonal flux coordinate system and the field-aligned coordinate system, where physical quantities are stored in the field-aligned coordinate system. In the quasi-ballooning coordinate system, spatial derivatives are evaluated on either the (ζ, ψ)-plane in the orthogonal flux coordinate system or the (y, z)-plane in the field-aligned coordinate system. It should be noted that ψ-derivative and y-derivative are not commutative due to the difference of the coordinate systems. This non-commutative property however doesn't make a problem since second-order partial derivatives $\partial_{\psi,y}^2$ and $\partial_{y,\psi}^2$ or $\partial_{x,y}^2$ and $\partial_{y,x}^2$ never appear in all differential operators used in this paper for the orthogonal property $g^{xy} = 0$. The other second-order partial derivatives relating to x-derivative can be rewritten as

$$\frac{\partial^2 f}{\partial x^2} = \frac{\partial^2 f}{\partial \psi^2} + 2I \frac{\partial^2 f}{\partial \psi \partial \zeta} + \frac{\partial I}{\partial \psi} \frac{\partial f}{\partial \zeta} + I^2 \frac{\partial^2 f}{\partial \zeta^2}, \tag{A18}$$

$$\frac{\partial^2 f}{\partial x \partial z} = \frac{\partial^2 f}{\partial z \partial x} = \frac{\partial^2 f}{\partial \psi \partial \zeta} + I \frac{\partial^2 f}{\partial \zeta^2}. \tag{A19}$$

The quasi-ballooning coordinate system employs the following shifted basis vectors $\boldsymbol{e}_{x_i}$ and $\boldsymbol{e}^{x_i}$ for $x_i = (u, v, w)$ rather than Eq. (A7) and Eq. (A8) in order to remove I from differential operators,

$$\boldsymbol{e}_u = \boldsymbol{e}_x - I\boldsymbol{e}_z, \quad \boldsymbol{e}_v = \boldsymbol{e}_y, \quad \boldsymbol{e}_w = \boldsymbol{e}_z, \tag{A20}$$

$$\boldsymbol{e}^u = \boldsymbol{e}^x, \quad \boldsymbol{e}^v = \boldsymbol{e}^y, \quad \boldsymbol{e}^w = \boldsymbol{e}^z + I\boldsymbol{e}^x, \tag{A21}$$

which gives the following shifted metrics

$$g_{x_i x_j} = \boldsymbol{e}_{x_i} \cdot \boldsymbol{e}_{x_j} = \begin{pmatrix} g_{\psi\psi} & 0 & 0 \\ 0 & g_{\theta\theta} + \nu^2 g_{\zeta\zeta} & \nu g_{\zeta\zeta} \\ 0 & \nu g_{\zeta\zeta} & g_{\zeta\zeta} \end{pmatrix}, \tag{A22}$$

$$g^{x_i x_j} = \boldsymbol{e}^{x_i} \cdot \boldsymbol{e}^{x_j} = \begin{pmatrix} g^{\psi\psi} & 0 & 0 \\ 0 & g^{\theta\theta} & -\nu g^{\theta\theta} \\ 0 & -\nu g^{\theta\theta} & \nu^2 g^{\theta\theta} + g^{\zeta\zeta} \end{pmatrix}. \tag{A23}$$

With these shifted basis vectors and metrics, terms including I in differential operators are canceled out so that vector calculus in the quasi-ballooning coordinate system can be written

without I. For example, the perpendicular Laplacian can be written as

$$\nabla_\perp^2 f = g^{uu}\frac{\partial^2 f}{\partial \psi^2} + g^{ww}\frac{\partial^2 f}{\partial \zeta^2} + G^u\frac{\partial f}{\partial \psi} + G^w\frac{\partial f}{\partial \zeta} + 2g^{vw}\frac{\partial^2 f}{\partial y \partial z}$$
$$+ \left(g^{vv} - \frac{1}{g_{vv}}\right)\frac{\partial^2 f}{\partial y^2} + \frac{1}{J}\left\{\frac{\partial}{\partial y}\left[J\left(g^{vv} - \frac{1}{g_{vv}}\right)\right]\right\}\frac{\partial f}{\partial y} \qquad \text{(A24)}$$

and the Poisson bracket can be also written as

$$\frac{\boldsymbol{b}_0 \times \nabla f \cdot \nabla g}{B} = \frac{\partial f}{\partial z}\frac{\partial g}{\partial \psi} - \frac{\partial f}{\partial \psi}\frac{\partial g}{\partial z} + \frac{g_{vw}}{g_{vv}}\left(\frac{\partial f}{\partial \psi}\frac{\partial g}{\partial y} - \frac{\partial f}{\partial y}\frac{\partial g}{\partial \psi}\right). \qquad \text{(A25)}$$

Appendix B: Poisson solvers in BOUT++

To reproduce the ELM crash including the complete set of $n = 0$ modes in the BOUT++ framework, we introduce the two-dimensional Poisson solver for $n = 0$ mode while the flute-ordered one-dimensional Poisson solver is still applied for $n \neq 0$ modes like Hermes code[29]. In this framework, the poloidal asymmetry of $n = 0$ mode and short wave-length modes can be handled without any numerical problems. However, it should be noticed that the flute-ordering assumption is not obvious for very long wave-length modes $\mathcal{O}(n) \sim 1$. Due to this issue, we set the computational domain to 1/5-th of annular torus with $N = 5$ to remove $1 \leq n \leq 4$ modes so that only $n = 0, 5, 10, \cdots, 160$ modes are taken in the present work.

1. Flute-ordered one-dimensional Poisson solver for $n \neq 0$ modes

As a first step for the two-dimensional Poisson solver for $n = 0$ mode, we briefly explain how the flute-ordered perpendicular Laplacian is implemented in the BOUT++ framework. The perpendicular Laplacian in the quasi-ballooning coordinate system Eq. (A24) has derivatives to be evaluated in both the orthogonal flux coordinate system and those in the field-aligned coordinate system. This is the reason why a Poisson solver in the quasi-ballooning coordinate system is not straightforwardly implemented as a boundary value problem. The original BOUT++ therefore employs the flute-order assumption $k_\parallel/k_\perp \ll 1$ which justifies to neglect y-derivatives from Eq. (A24) and gives

$$\nabla_\perp^2 f = g^{uu}\frac{\partial^2 f}{\partial \psi^2} + g^{ww}\frac{\partial^2 f}{\partial \zeta^2} + G^u\frac{\partial f}{\partial \psi} + G^w\frac{\partial f}{\partial \zeta}. \qquad \text{(B1)}$$

Now all the derivatives in Eq. (B1) can be evaluated in the orthogonal flux coordinate system so that the flute-ordered Poisson solver corresponding to Eq. (B1) can be defined as a boundary value problem in the orthogonal flux coordinate system. For consistency between the forward operator $\nabla_\perp^2$ and the backward operator $\nabla_\perp^{-2}$, the original BOUT++ employs the flute-ordered perpendicular Laplacian Eq. (B1) rather than the full perpendicular Laplacian Eq. (A24). Since physical quantities are stored in the field-aligned coordinate system, the flute-ordered perpendicular Laplacian is evaluated in the Fourier space associated with the toroidal angle ζ as

$$\nabla_\perp^2 f = \mathcal{F}^{-1}\left\{\left[\nabla_\perp^2\left(\mathcal{F}\{f\} e^{-in\alpha}\right)\right] e^{in\alpha}\right\} = \mathcal{F}^{-1}\left\{\left(\nabla_\perp^2 F\right) e^{in\alpha}\right\}, \tag{B2}$$

$$\nabla_\perp^2 F = g^{uu}\frac{\partial^2 F}{\partial \psi^2} + (in)^2 g^{ww} F + G^u \frac{\partial F}{\partial \psi} + inG^w F, \tag{B3}$$

where Eq. (B3) is discretized with second-order central differencing schemes in ψ-direction.

For the flute-ordered Poisson solver, the following Helmholtz equation for a three-dimensional field f with two-dimensional coefficients $d(x,y)$, $c(x,y)$, $a(x,y)$ and a right-hand-side field $b(x,y,z)$ is implemented in the BOUT++ framework

$$d\nabla_\perp^2 f + \frac{1}{c}\nabla c \cdot \nabla_\perp f + af = b. \tag{B4}$$

This equation can be reduced to the one-dimensional boundary value problem for each toroidal mode n

$$dg^{uu}\frac{\partial^2 F}{\partial \psi^2} + \left(dG^u + \frac{g^{uu}}{c}\frac{\partial c}{\partial \psi}\right)\frac{\partial F}{\partial \psi} + \left(a - dn^2 g^{ww} + indG^w\right) F = \mathcal{F}\{b\} e^{-in\alpha}, \tag{B5}$$

where y derivative of coefficient c has not been implemented in BOUT++ so far. Eq. (B5) is also discretized with second-order central differencing schemes in ψ-direction and solved with Thomas tridiagonal algorithm.

2. Two-dimensional Poisson solver for $n = 0$ mode

Application of Eq. (B5) for $n = 0$ mode causes disruptive numerical noise in the magnetic field line direction since the flute-order assumption is not applicable for $n = 0$ mode. Mathematically speaking, the flute-ordered Poisson solver cannot reproduce the poloidal structure of F for $n = 0$ mode since it is reduced to the one-dimensional boundary value problem in ψ-direction. To resolve this problem, the two-dimensional Poisson solver for $n = 0$ mode

$$d\nabla_\perp^2 \bar{f} + \frac{1}{c}\nabla c \cdot \nabla_\perp \bar{f} + a\bar{f} = \bar{b}, \tag{B6}$$

is introduced in the BOUT++ framework like Hermes code, where $\bar{f}$ represents the $n = 0$ component of the variable f. The reason why the two-dimensional Poisson solver is available for $n = 0$ mode is that $n = 0$ component of $f(x, y, z)$ and that of $f(\psi, \theta, \zeta)$ are mathematically identical for

$$\frac{\partial \bar{f}}{\partial x} = \frac{\partial \bar{f}}{\partial \psi} + I \frac{\partial \bar{f}}{\partial \zeta} = \frac{\partial \bar{f}}{\partial \psi}, \tag{B7}$$

$$\frac{\partial \bar{f}}{\partial y} = \frac{\partial \bar{f}}{\partial \theta} + \nu \frac{\partial \bar{f}}{\partial \zeta} = \frac{\partial \bar{f}}{\partial \theta}. \tag{B8}$$

With the shifted metrics Eq. (A22) and Eq. (A23) and the relations Eq. (B7) and Eq. (B8), the Helmholtz equation Eq. (B6) finally gives

$$dg^{uu} \frac{\partial^2 \bar{f}}{\partial x^2} + \left(dG^u + \frac{g^{uu}}{c} \frac{\partial c}{\partial x} \right) \frac{\partial \bar{f}}{\partial x}$$
$$+ d \left(g^{vv} - \frac{1}{g_{vv}} \right) \frac{\partial^2 \bar{f}}{\partial y^2} + \frac{d}{J} \frac{\partial}{\partial y} \left[J \left(g^{vv} - \frac{1}{g_{vv}} \right) \right] \frac{\partial \bar{f}}{\partial y} + a\bar{f} = \bar{b}, \tag{B9}$$

which is equivalent to Eq. (B6) expressed in the flux orthogonal coordinate system. Eq. (B9) is discretized with second-order central differencing schemes in x-direction and y-direction and is solved with PETSc library[45–47] as a two-dimensional boundary value problem. For the consistency with the Poisson solvers Eq. (B5) and Eq. (B9), the perpendicular Laplacian implemented in the original BOUT++ Eq. (B1) is then modified to

$$\nabla_\perp^2 f = g^{uu} \frac{\partial^2 f}{\partial \psi^2} + g^{ww} \frac{\partial^2 f}{\partial \zeta^2} + G^u \frac{\partial f}{\partial \psi} + G^w \frac{\partial f}{\partial \zeta}$$
$$+ \left(g^{vv} - \frac{1}{g_{vv}} \right) \frac{\partial^2 \bar{f}}{\partial y^2} + \frac{1}{J} \frac{\partial}{\partial y} \left[J \left(g^{vv} - \frac{1}{g_{vv}} \right) \right] \frac{\partial \bar{f}}{\partial y}. \tag{B10}$$

It should be noted that the fifth term in Eq. (A24) is not taken in the proposed scheme from the view point of consistency between the forward and the backward operator. To introduce this term, a novel two-dimensional Poisson solver must be required to invert Eq. (B4) including y-derivatives for resonant modes, which may have a considerable impact on very-low-n modes. It is left as a future work.

REFERENCES

[1]A. Loarte, B. Lipschultz, A. S. Kukushkin, G. F. Matthews, P. C. Stangeby, N. Asakura, G. F. Counsell, G. Federici, A. Kallenbach, K. Krieger, A. Mahdavi, V. Philipps, D. Reiter, J. Roth, J. Strachan, D. Whyte, R. Doerner, T. Eich, W. Fundamenski, A. Herrmann,

M. Fenstermacher, P. Ghendrih, M. Groth, A. Kirschner, S. Konoshima, B. LaBombard, P. Lang, A. W. Leonard, P. Monier-Garbet, R. Neu, H. Pacher, B. Pegourie, R. A. Pitts, S. Takamura, J. Terry, E. Tsitrone, t. I. S.-o. L. Group, and Diver, Nuclear Fusion **47**, S203 (2007).

[2] R. Wenninger, R. Kembleton, C. Bachmann, W. Biel, T. Bolzonella, S. Ciattaglia, F. Cismondi, M. Coleman, A. J. H. Donné, T. Eich, E. Fable, G. Federici, T. Franke, H. Lux, F. Maviglia, B. Meszaros, T. Pütterich, S. Saarelma, A. Snickers, F. Villone, P. Vincenzi, D. Wolff, and H. Zohm, Nuclear Fusion **57**, 016011 (2016).

[3] N. Asakura, K. Hoshino, S. Suzuki, S. Tokunaga, Y. Someya, H. Utoh, H. Kudo, Y. Sakamoto, R. Hiwatari, K. Tobita, K. Shimizu, K. Ezato, Y. Seki, N. Ohno, Y. Ueda, and Joint Special Team for DEMO Design, Nuclear Fusion **57**, 126050 (2017).

[4] F. Wagner, G. Becker, K. Behringer, D. Campbell, A. Eberhagen, W. Engelhardt, G. Fussmann, O. Gehre, J. Gernhardt, G. v. Gierke, G. Haas, M. Huang, F. Karger, M. Keilhacker, O. Klüber, M. Kornherr, K. Lackner, G. Lisitano, G. G. Lister, H. M. Mayer, D. Meisel, E. R. Müller, H. Murmann, H. Niedermeyer, W. Poschenrieder, H. Rapp, H. Röhr, F. Schneider, G. Siller, E. Speth, A. Stäbler, K. H. Steuer, G. Venus, O. Vollmer, and Z. Yü, Physical Review Letters **49**, 1408 (1982).

[5] H. Zohm, Plasma Physics and Controlled Fusion **38**, 1213 (1999).

[6] X. Q. Xu and R. H. Cohen, Contributions to Plasma Physics **38**, 158 (1998).

[7] X. Q. Xu, R. H. Cohen, T. D. Rognlien, and J. R. Myra, Physics of Plasmas **7**, 1951 (2000).

[8] X. Q. Xu, M. V. Umansky, B. D. Dudson, and P. B. Snyder, Communications in Computational Physics **4**, 949 (2008).

[9] M. V. Umansky, X. Q. Xu, B. Dudson, L. L. LoDestro, and J. R. Myra, Computer Physics Communications **180**, 887 (2009).

[10] W. Park, E. V. Belova, G. Y. Fu, X. Z. Tang, H. R. Strauss, and L. E. Sugiyama, Physics of Plasmas **6**, 1796 (1999).

[11] C. R. Sovinec, A. H. Glasser, T. A. Gianakon, D. C. Barnes, R. A. Nebel, S. E. Kruger, D. D. Schnack, S. J. Plimpton, A. Tarditi, and M. S. Chu, Journal of Computational Physics **195**, 355 (2004).

[12] A. Y. Pankin, G. Bateman, D. P. Brennan, A. H. Kritz, S. Kruger, P. B. Snyder, C. Sovinec, and the NIMROD team, Plasma Physics and Controlled Fusion **49**, S63 (2007).

[13]G. T. A. Huysmans and O. Czarny, Nuclear Fusion **47**, 659 (2007).

[14]O. Czarny and G. Huysmans, Journal of Computational Physics **227**, 7423 (2008).

[15]S. Pamela, G. Huysmans, and S. Benkadda, Plasma Physics and Controlled Fusion **52**, 075006 (2010).

[16]F. Orain, M. Becoulet, G. Dif-Pradalier, G. Huijsmans, S. Pamela, E. Nardon, C. Passeron, G. Latu, V. Grandgirard, A. Fil, A. Ratnani, I. Chapman, A. Kirk, A. Thornton, M. Hoelzl, and P. Cahyna, Physics of Plasmas **20**, 102510 (2013).

[17]F. Orain, M. Becoulet, G. T. A. Huijsmans, G. Dif-Pradalier, M. Hoelzl, J. Morales, X. Garbet, E. Nardon, S. Pamela, C. Passeron, G. Latu, A. Fil, and P. Cahyna, Physical Review Letters **114**, 035001 (2015).

[18]J. A. Morales, M. Becoulet, X. Garbet, F. Orain, G. Dif-Pradalier, M. Hoelzl, S. Pamela, G. T. A. Huijsmans, P. Cahyna, A. Fil, E. Nardon, C. Passeron, and G. Latu, Physics of Plasmas **23**, 042513 (2016).

[19]N. M. Ferraro, S. C. Jardin, and P. B. Snyder, Physics of Plasmas **17**, 102508 (2010).

[20]B. D. Dudson, M. V. Umansky, X. Q. Xu, P. B. Snyder, and H. R. Wilson, Computer Physics Communications **180**, 1467 (2009).

[21]B. D. Dudson, X. Q. Xu, M. V. Umansky, H. R. Wilson, and P. B. Snyder, Plasma Physics and Controlled Fusion **53**, 054005 (2011).

[22]X. Q. Xu, B. Dudson, P. B. Snyder, M. V. Umansky, and H. Wilson, Physical Review Letters **105**, 949 (2010).

[23]X. Q. Xu, T. Y. Xia, N. Yan, Z. X. Liu, D. F. Kong, A. Diallo, R. J. Groebner, A. E. Hubbard, and J. W. Hughes, Physics of Plasmas **23**, 055901 (2016).

[24]H. Jhang, H. H. Kaang, S. S. Kim, T. Rhee, R. Singh, and T. S. Hahm, Nuclear Fusion **57**, 022006 (2017).

[25]J. Kim, W. Lee, H. Jhang, S. S. Kim, H. H. Kaang, and Y. c. Ghim, Physics of Plasmas **25**, 082306 (2018).

[26]R. Z. Sagdeev, V. D. Shapiro, and V. I. Shevchenko, Soviet Journal of Plasma Physics **4**, 551 (1978).

[27]P. H. Diamond, S. I. Itoh, K. Itoh, and T. S. Hahm, Plasma Physics and Controlled Fusion **47**, R35 (2005).

[28]S. Nishimura, S. Benkadda, M. Yagi, S. I. Itoh, and K. Itoh, Physics of Plasmas **15**, 092506 (2008).

[29] B. D. Dudson and J. Leddy, Plasma Physics and Controlled Fusion **59**, 054010 (2017).

[30] R. D. Hazeltine, M. Kotschenreuther, and P. J. Morrison, Physics of Fluids **28**, 2466 (1985).

[31] Z. Chang and J. D. Callen, Physics of Fluids B: Plasma Physics **4**, 1766 (1992).

[32] S. D. Cohen and A. C. Hindmarsh, COMPUTERS IN PHYSICS **10**, 138 (1996).

[33] G. D. Byrne and A. C. Hindmarsh, The International Journal of High Performance Computing Applications **13**, 354 (1999).

[34] R. L. Miller and J. W. Vandam, Nuclear Fusion **27**, 2101 (1987).

[35] B. J. Burke, S. E. Kruger, C. C. Hegna, P. Zhu, P. B. Snyder, C. R. Sovinec, and E. C. Howell, Physics of Plasmas **17**, 032103 (2010).

[36] G. Y. Park, S. S. Kim, H. Jhang, P. H. Diamond, T. Rhee, and X. Q. Xu, Physics of Plasmas **22**, 032505 (2015).

[37] N. Winsor, J. L. Johnson, and J. M. Dawson, Physics of Fluids **11**, 2448 (1968).

[38] T. S. Hahm and K. H. Burrell, Physics of Plasmas **2**, 1648 (1995).

[39] K. H. Burrell, Physics of Plasmas **4**, 1499 (1997).

[40] J. Cheng, J. Q. Dong, K. Itoh, L. W. Yan, M. Xu, K. J. Zhao, W. Y. Hong, Z. H. Huang, X. Q. Ji, W. L. Zhong, D. L. Yu, S. I. Itoh, L. Nie, D. F. Kong, T. Lan, A. D. Liu, X. L. Zou, Q. W. Yang, X. T. Ding, X. R. Duan, and Y. Liu, Physical Review Letters **110**, 265002 (2013).

[41] E.-j. Kim and P. H. Diamond, Physical Review Letters **90**, 313 (2003).

[42] W. D. D'haeseleer, W. N. G. Hitchon, J. D. Callen, and J. L. Shohet, Flux Coordinates and Magnetic Field Structure (Springer-Verlag, 1991).

[43] A. M. Dimits, Physical Review E **48**, 4070 (1993).

[44] B. Scott, Physics of Plasmas **8**, 447 (2001).

[45] S. Balay, S. Abhyankar, M. F. Adams, J. Brown, P. Brune, K. Buschelman, L. Dalcin, V. Eijkhout, W. D. Gropp, D. Kaushik, M. G. Knepley, D. A. May, L. C. McInnes, K. Rupp, B. F. Smith, S. Zampini, H. Zhang, and H. Zhang, "PETSc Web page," `http://www.mcs.anl.gov/petsc` (2017).

[46] S. Balay, S. Abhyankar, M. F. Adams, J. Brown, P. Brune, K. Buschelman, L. Dalcin, V. Eijkhout, W. D. Gropp, D. Kaushik, M. G. Knepley, D. A. May, L. C. McInnes, K. Rupp, P. Sanan, B. F. Smith, S. Zampini, H. Zhang, and H. Zhang, "PETSc users manual," Tech. Rep. ANL-95/11 - Revision 3.8 (Argonne National Laboratory, 2017).

[47]S. Balay, W. D. Gropp, L. C. McInnes, and B. F. Smith, in <u>Modern Software Tools in Scientific Computing</u>, edited by E. Arge, A. M. Bruaset, and H. P. Langtangen (Birkhäuser Press, 1997) pp. 163–202.